

Development of a prototype autonomous inspection robot for offshore riser cables

Christopher Gotts^a, Benjamin Hall^a, Oliver Beaumont^a, Ziyang Chen^a, William Cleaver^a, James England^a, David White^a and Blair Thornton^{a,b,*}

^aUniversity of Southampton, University Road, Southampton, SO17 1BJ, UK

^bInstitute of Industrial Science, The University of Tokyo, Komaba 4-6-1, Tokyo 153-8505, Japan

ARTICLE INFO


Keywords:
Robotic Inspection
Autonomy
Sensing and Computer Vision
Offshore Riser Cables
Floating Offshore Wind

ABSTRACT

The motion and large environmental loads experienced by riser cables connected to floating offshore wind turbines put them at higher risk of failure than grounded sections of cable. We propose an Autonomous Riser Inspection System (ARIS) to facilitate regular inspection of riser cables for early fault detection and gathering engineering data to improve future cable design. Novel robotic methods for automatic attachment, traversal and inspection of cables are described. We develop the sensing and intelligent processing needed to (i) enable autonomous traversal and position estimation, and (ii) gather information about the state and condition of riser cables. Information from an array of cameras and electric actuator current monitoring allows autonomous navigation around obstacles and identifying the end of the inspection. A visual processing algorithm identifies damage to the surface of the cable and sensing methods are developed to measure the cable catenary, where methods to estimate the robot's position along the cable are developed to contextualise and efficiently re-locate observations. Technology concepts are verified through a combination of dry, lab-based experiments using a full-scale prototype and simulations. The results provide proof the concept that requirements for untethered, autonomous riser cable inspection can be met by the proposed system.

1. Introduction

Offshore wind farms are growing in size, number, and remoteness from shore to meet global carbon emissions targets (IRENA, 2021). Floating offshore wind turbines can access stronger winds in deeper, less congested waters than fixed monopiles, making them an important technology for future clean energy generation (UK Government, 2020). However, an increase in the scale of offshore wind needs to be matched by high reliability of the component technologies, where ~90 % of failures currently relate to the high power cables that connect offshore wind to the electricity grid (Proskovics, 2017). If a subsea power cable fails, the average cost of repair including lost revenue is approximately £20 million, where this reduces to approximately £5 million for pre-emptive repairs identified through inspection (McKeever and Young, 2020). Reliability data for floating offshore wind is limited because full-scale platforms have only been operational since 2017 (Young, 2018). However, more than half of failures in static power cables that connect fixed offshore assets are caused by gradual processes such as abrasion (21.7%) and corrosion (16.7%) of the cable armour that can potentially be identified through regular inspection (Dinmohammadi et al., 2019). The exposure to high-energy environments and more complex dynamics of floating wind platforms cause riser cables to experience greater stresses than static cables (Young et al., 2018). Simulations by McKeever and Young (2020)

 b.thornton@soton.ac.uk (B. Thornton)
ORCID(s):

41 showed that riser cables have an increased risk of failure due to abrasion and fatigue, predicting the average lifetime
42 of current riser designs to be in the order of 10-12 years, approximately half of their design life. Barriers to improving
43 floating offshore wind reliability include:

- 44 • Lack of knowledge on how dynamic riser cables behave and fail in service
- 45 • Preventable cable failures due to missed symptoms of gradual failure mechanisms

46 Although both points can be addressed through regular inspection and monitoring of in service riser cables, traditional
47 inspection methods using Remotely Operated Vehicles (ROVs) and human divers are expensive, have low repeatability
48 and often generate incomplete data (Campos et al., 2021). Inspection by divers is slow and risks human safety. For
49 camera equipped ROVs, the risk of entanglement with the ROV tether means that typically only one perspective
50 of the cable is observed, leaving the risk of critical damage symptoms being missed on the obscured 180° of cable
51 surface. ROVs, trained pilots and divers are typically available on-board offshore oil and gas platforms, making their
52 use convenient. This is not the case for offshore wind, where the platforms are uncrewed and so inspection requires
53 dedicated equipment and service provisions. The aim of this paper is to demonstrate the technology concepts needed to
54 enable efficient, low-cost autonomous robotic inspection of offshore riser cables. The inspection system described here
55 aims to gather information about riser dynamics and failure mechanisms, enabling pre-emptive repair and informing
56 optimised design, ultimately improving the reliability of offshore wind.

57 The rest of this paper is organised as follows. Section 2 presents the overall concept for autonomous cable
58 inspection, identifying the requirements of the proposed robotic inspection method and scope of investigations in this
59 paper. We present the concept and subsystems designed to meet these objectives in Sections 3 to 6. Section 7 validates
60 the performance of a full-scale prototype robot in a series of dry laboratory-based experiments and simulations that
61 demonstrate the key capabilities needed to automate riser cable inspection. Section 8 draws conclusions and identifies
62 requirements for further concept development.

63 **2. Concept Design**

64 **2.1. Workflow and Scope**

65 The dynamic nature of a riser cable complicates inspection as it is necessary to traverse a moving target while
66 maintaining sufficiently close range to make observations, and also keep track of where each observation is made
67 along the length of the cable. One strategy to simplify both close traversal and self-localisation is to physically attach
68 a mobile inspection robot to the riser cable. Once deployed near the target riser cable, the system must attach to it,
69 traverse its length while performing inspection and location tracking, and finally detach itself from the cable once the
70 inspection is complete so that it can be retrieved, as illustrated in Figure 1.

Autonomous deployment and retrieval is possible using technology that exists in commercial Autonomous Underwater Vehicles (AUVs), which are capable of self-propelled navigation underwater. The accurate relative positioning needed prior to attachment of a system has been demonstrated by several groups in recent docking research (Matsuda et al., 2019). Similarly, technology for a submerged robotic platform to resurface using variable buoyancy or drop weights (Thornton, 2020; Rolfe et al., 2020), and send location information (e.g., via iridium satellites) to enable recovery are well established and implemented on most autonomous underwater platforms (Zolich et al., 2019).

This paper focuses on developing novel methods for the autonomous attachment, traversal, inspection and detachment stages of the workflow that have not previously been demonstrated. The objectives are to design and demonstrate:

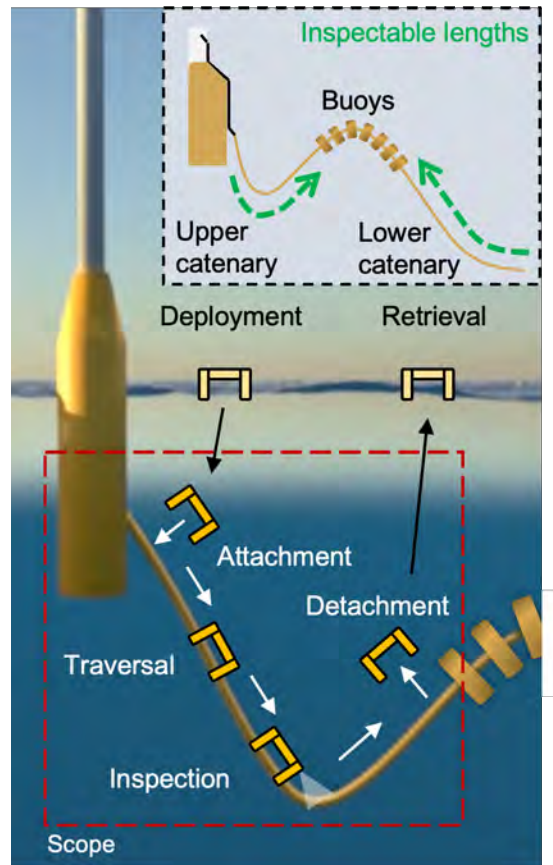


Figure 1: Mobile inspection workflow. Once deployed, the system must be capable of; attachment, traversal, inspection and detachment, before retrieval. The inset is a wider view of an entire riser cable, adapted from (Eldøy, 2017). The exposed sections of riser targeted for inspection in this work are highlighted with green arrows. The locations of the start of the arrows (i.e., near surface, near seabed) would typically be defined. For the risers used in the Hywind floating offshore wind farm, the upper and lower inspectable riser sections are 125 m and 55 m long, respectively. Traversing in the direction of the arrow would terminate at the buoyancy blocks used between the upper and lower riser catenary sections.

- Physical traversal of a riser cable and ability to withstand expected disturbance
- Behaviours needed for robust autonomous operation
- Sensor systems to gather inspection data

Experiments have been designed to demonstrate the feasibility of each subsystem under dry test conditions and simulation, highlighting where appropriate any significant differences from conditions expected during underwater operation.

2.2. Design Requirements

Riser cables typically range in diameter from 150 mm to 200 mm (Eldøy, 2017), with a damage inducing minimum bend radius of around 2 m (Rentschler et al., 2019). Inspection is feasible anywhere the cable surface is not obscured by buoyancy devices or sheaths. The longest exposed riser sections for current operational floating offshore wind farms are between 110 m and 125 m. A robotic inspection system must be capable of traversing a riser cable under these conditions without damaging the cable, and must be robust to expected disturbance forces and accelerations from waves and currents, and changes in cable profile and friction due to marine growth. Furthermore, the system must be able to attach itself to the cable in the presence of small uncertainties in its relative position.

AUVs have demonstrated relative positioning accuracies of 100 mm at sea in currents of 0.5 m.s^{-1} during docking experiments (Matsuda et al., 2019). Based on this we set a design target for attachment to be possible for $\pm 50 \text{ mm}$ offset in relative position to the centre of riser cables with a diameter of 150 mm to 200 mm. This is reasonable considering that the mean current velocities in the North Sea, where the Hywind and other future floating offshore wind farms are located, are below 0.05 m.s^{-1} , with peaks of generally no more than 0.2 m.s^{-1} (Global Monitoring and Forecasting Center, 2021).

Once attached, one strategy is to use friction between the inspection robot and the cable surface for traversal. The material used for the external surface of the riser cables is a typically a proprietary High Density Polyethylene (HDPE), HE 6063 (Eldøy, 2017), which has a friction coefficient of 0.057 with rubber in seawater. Although build-up of algae on the cable surface can reduce friction at the interface, solutions for brush-based and ultrasonic cleaning of subsea infrastructure could potentially be adapted to remove biological films without risking damage to the cable material (Song and Cui, 2020; Albitar et al., 2016). In order to avoid damaging the cable, it is necessary to limit the pressure the inspection robot applies to the cable surface to below half the yield stress of HE 6063, 6.9 MPa (MatWeb, 2021).

To operate autonomously, the system needs to be capable of detecting the riser cable once it is in a suitable position so that it can initially attach itself. During traversal the system must be capable of navigating past small obstacles and

111 surface growth, such as barnacles (typically ~ 15 mm in size (White, 2008)) and any change in cable diameter within
112 its design envelope. The system also needs to be able to identify large obstacles, recognising when these cannot be
113 passed so that it can detach itself for early recovery. In normal operation, missions will end when the system reaches
114 buoyancy modules. These should also be automatically detected so the system is aware the mission is complete.

115 A successful inspection requires coverage of 360° around the cable circumference along the entire cable length.
116 The system should be able to autonomously identify and flag areas with surface damage. Whilst research suggests
117 that micrometre scale defects can be initiation sites for failure through electrical treeing (Young, 2018), our target
118 is to gather full-field data at resolutions similar to current ROV and diver surveys, and so we set a 0.5 mm target
119 for automatic damage detection. Removal of surface growth using methods such as those described in Song and Cui
120 (2020) and Albitar et al. (2016) may be necessary for detection of small defects in bio-fouled cable surfaces. Collecting
121 information about the shape of the cable along its length is also valuable to identify areas of tight bends, and to provide
122 data of the in-operation geometry to support load and fatigue reassessments, to check for the risk of unpredicted
123 accelerated failure. To contextualise both outputs, the system must also be able to estimate its position along the cable.
124 This should be done with sufficient accuracy to allow for identified locations to be efficiently identified for maintenance
125 or repair. We set a target accuracy of locating observations to within 5 m of their actual position along the length of the
126 cable, as this would allow flagged areas to be quickly relocated by divers and ROV pilots for maintenance operations.

127 **2.3. Design Precedents**

128 The requirement for close proximity, high resolution and 360° observation and need to measure the shape of the
129 cable make physical attachment a practical approach for inspection, with advantages over remote observation by an
130 ROV or diver, both of which offer reduced observation and localisation accuracy. This section reviews literature on
131 mobile robotic systems that physically attach to their inspection targets.

132 Bonnin-Pascual and Ortiz (2019) reviews state-of-the-art robotic ship hull inspection technology. These inspection
133 platforms identify cracks and damage on the submerged surface of ship hulls, coupling observations with position
134 information. Different challenges are identified for flat and curved surface inspection. Mechanisms for attachment
135 include suction and magnetism, though these are only suitable for relatively flat and ferrous surfaces, respectively.
136 Hachicha et al. (2019) investigates how the centre of buoyancy can be used to achieve a pendulum effect that enhances
137 platform stability under the reaction forces from the water nozzles when operating on hull surfaces. In BladeBUG
138 (2021), the authors propose a system that uses six suction pad feet to adapt to complex geometries on the curved
139 surfaces of wind turbines, where semi-autonomous operation is proposed to reduce the human input required during
140 inspection. Although these methods are effective on relatively flat surfaces like a ship's hull or wind turbine blades,
141 their use for cable inspection is limited. Figure 2a illustrates how suction based methods would struggle with the high

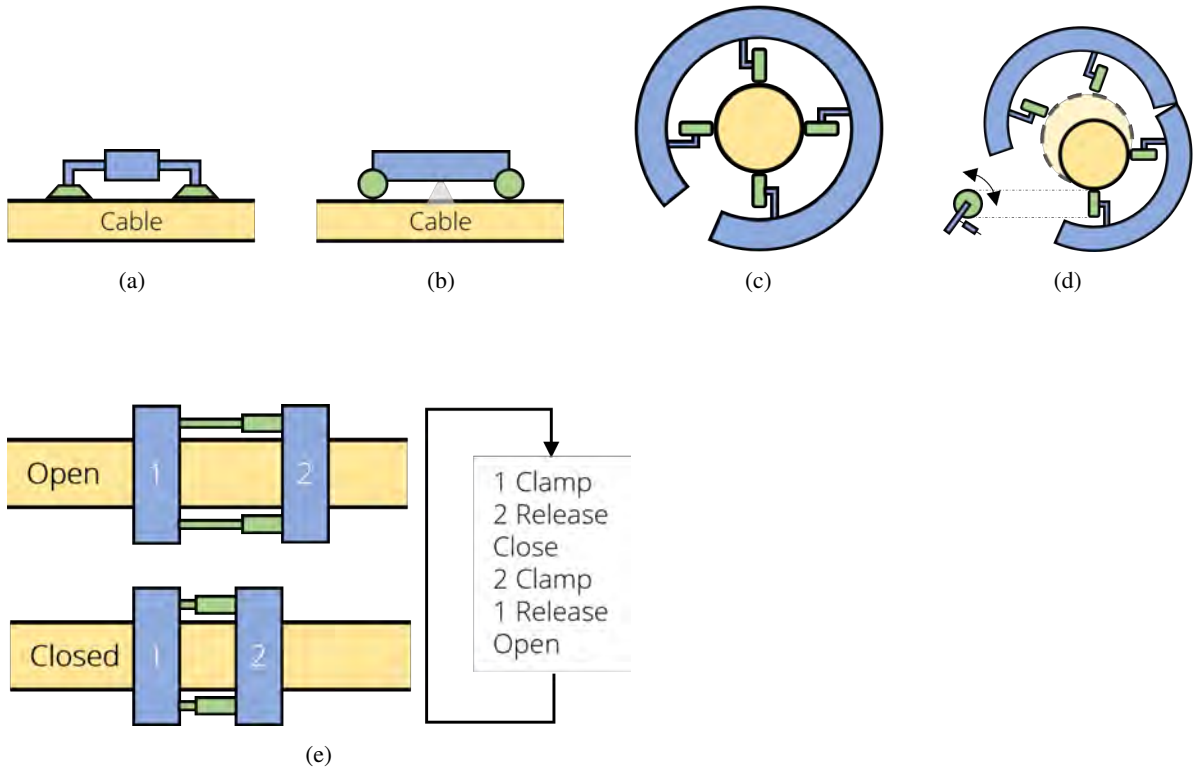


Figure 2: Concept sketches showing possible implementations of the design precedents available in literature to the challenge of inspecting riser cables. (a) Suction pads for attachment, (b) magnetic wheels for attachment and traversal on ferrous targets, (c) enveloping wheels for 360° inspection and traversal, (d) sprung enveloping wheels for variable cable diameters, and (e) clamp and push for 360° inspection and traversal.

curvature of cable surfaces, and the use of buoyancy is complicated by the presence of both horizontal and vertical riser sections. Boenisch (2015) presents inspection methods that are more suited to the curved geometry of riser cables. The MEC Combi Crawler, illustrated in Figure 2b, uses wheels to roll along the pipe, enabling efficient motion at high speeds. The system uses magnetic forces to maintain contact with ferrous pipes. However, riser cables are typical non-ferrous, making magnetic attachment infeasible. Even so, the large curvature of the cable cross sections means that compact systems can still grip around a cable, greatly simplifying attachment and traversal related challenges, and also making it easier to obtain a 360° view of the cable surface.

In Bonnin-Pascual and Ortiz (2019), the authors identify a trend from teleoperated ROVs towards autonomous inspection using AUVs. For these systems, the use of vision is becoming increasingly established as an effective and flexible solution for sensing that can enable automation of complex behaviours, while also generating useful inspection data. Vision systems tend to require precise control of the distance between the cameras and inspection target, combined with artificial lighting to achieve robust performance (Thornton et al., 2016). Processing of visual images using standard methods such as Canny edge detection can be used for crack detection (Bonnin-Pascual and Ortiz, 2019). Several studies

155 have used machine learning for increased detection accuracy, achieving crack detection levels of 72% with a 27% false
156 positive rate. Various strategies have been proposed to localise observation of infrastructure, including the use of vision
157 systems, Inertial Measurement Units (IMUs), depth sensors and Doppler Velocity Logs (DVLs) for self-localisation, all
158 of which could be applied to cable inspection. These methods work by measuring relative motions that are integrated to
159 compute the platform's trajectory. However, these approaches suffer from error accumulation, with various approaches
160 including the use of Simultaneous Localisation and Mapping (SLAM) techniques being adopted to address this issue.
161 Other localisation methods use external landmarks in the form of acoustic beacons or magnetic targets, which can
162 allow for direct measurement of the relative location of an observation, but at the cost of operational complexity since
163 the position of the landmarks themselves need to be well characterised. In the majority of cases, data from multiple
164 sensors is fused using variants of the Kalman filter in order to improve the accuracy of location estimates.

165 Kaur et al. (2018) describe a radiographic tool called RiserSure for inspection of vertical flexible pipe risers. The
166 proposed system grips the cable by wrapping around it for a secure connection. This enables a 360° measurements
167 to be made. The system developed in Kaur et al. (2018) is however not capable of traversal under its own actuation,
168 instead making use of a winch on the water surface to control its position. The system requires permanent operator
169 supervision, making use of retracting point grippers to secure the system to the cable when making observations. A
170 potential adaptation of this concept with the addition of wheels for efficient motion is shown in Figure 2c. However,
171 RiserSure mounts its sensor suite on a circular track that completely encloses the cable, which complicates automation
172 of the initial attachment. Boenisch (2015) presents the MEC-FIT system that is also suited to use on cables that have
173 a large curvature. A wide opening allows for ROV deployment, where the MEC-FIT system encircles the cable to
174 prevent accidental detachment. However, for cable inspection, the proposed concept would need extending to address
175 a range of diameters, and less complex actuation methods are needed to improve the robustness of the initial attachment.
176 Figure 2d illustrates how this concept could potentially be modified with the addition of sprung wheels to accept a range
177 of cable diameters, where a similar concept is used in the SIRIS propeller driven riser pipe inspection robot developed
178 in Santos et al. (2013).

179 Singh and Ananthasuresh (2013) describes a clamp and push traversal system, illustrated in Figure 2e. During each
180 drive cycle, a secure connection is maintained with the cable by one of the two jaws. This is potentially beneficial
181 for autonomy because having one jaw clamped to the cable eliminates uncertainty from the system's motion, where a
182 properly designed system would reduce the probability of the system slipping, rotating or accidentally detaching. The
183 design can also accommodate a range of cable diameters. The system described by Singh and Ananthasuresh (2013)
184 has a low traversal speed of $2.7 \text{ m} \cdot \text{s}^{-1}$, which needs to be made much faster for inspection of $>10 \text{ m}$ lengths of cable
185 targeted in this work. In Kimball et al. (2018), the authors demonstrate the feasibility of this clamp and push concept
186 to traverse the mooring chains used to fix floating offshore structures. To address the complex chain geometry, a 90°

187 rotation of the two jaws was introduced between drive cycles. This feature is not required for riser cables where the
188 geometry is rotationally symmetric about the centerline. An advantage of this design is that it can accommodate a large
189 opening needed to simplify the attachment and detachment mechanics, and still traverse a cable using the clamping
190 pressure to remain attached.

191 **3. Design Proposal**

192 The proposed design is referred to as the Autonomous Riser Inspection System (ARIS). ARIS adapts the clamp and
193 push drive method shown in Singh and Ananthasuresh (2013) and Kimball et al. (2018) for traversal. Figure 3 shows
194 the overall design of ARIS, with key specifications given in Table 1. The shape of the jaws to clamp onto the cable use
195 a set of passive spring-loaded rollers to stabilise the platform and stay centred around a range of cable diameters during
196 the phases of the drive cycle when the drive actuator extends (DE) (push), and when the drive actuator contracts (DC)
197 (pull) (Figure 3). This is important for smooth traversal, and also to maintain an optimum position of the sensors used by
198 the system for inspection. The design uses three electrically powered linear actuators to open and close each of the two
199 jaws, and to extend and shorten the backbone of the system. To protect the cable from damage, compliant materials are
200 used on the surfaces of the jaws, and the force that is applied during clamping is monitored using calibrated electrical
201 current measurements so that the pressure applied does not exceed the yield stress of cable's outer material. The limit
202 is set to half of the yield stress to ensure damage does not occur. Further details of the design and traversal method are
203 discussed in section 4.

204 In addition to the physical attributes, it is necessary for the system to autonomously complete a full inspection with
205 no human input. The motivation for this is to avoid the requirement to tether the system, since tethers are prone to
206 entanglement especially in dynamic, high energy underwater environments and this would also require continuous
207 support of a crewed vessel during the inspection phase, greatly increasing the operational cost of a survey. The
208 possibility of acoustic communications was considered, but the low-communication bandwidths (typically <9.6 kbps)
209 and poor reliability of acoustic communication around built infrastructure introduces significant complications, which
210 can be avoided if the necessary autonomous behaviours can be developed. Although surface support is needed for
211 deployment and positioning for initial attachment, and to recover the system after inspection, this surface vessel is free
212 to perform other tasks or deploy additional units during the traversal and inspection phases of a survey. These phases
213 are expected to take between 2 h and 6 h for exposed lower and upper riser catenary sections of comparable length to
214 Hywind, respectively (see Figure 1). For this autonomous operation, the system must:

- 215 • Automatically detect and attach to the riser cable when in the initial position
- 216 • Adapt its drive sequence to overcome small obstacles on the cable's surface

Table 1
Basic specifications.

Name	Value	Unit
Length (max)	870	mm
Width (max)	650	mm
Height (max)	400	mm
Mass	23.2	kg
Inspection rate	~24	m.h ⁻¹
Cable diameter	160 to 210	mm
Prototype bill of materials	1100	£

- Identify when an obstacle is impassable and detach for recovery
- Detect the end of inspection automatically and detach for recovery

The methods to achieve these behaviours are discussed in section 5.

To gather inspection data, an array of four cameras with on-board lighting are used to capture a 360° video of the full length of traversed cable. Footage from the camera array is analysed to automatically highlight areas with visible anomalies on the cable surface, and is also used to estimate traversed distance using visual odometry. The motion estimates from the visual odometry are fused with the data from a linear potentiometer that measures the extension of the actuator between the front and rear jaws and, if necessary, the integrated measurements of vehicle acceleration made using an IMU. Data is fused using a Kalman Filter (KF), which is described in section 6.3. Tagging surface anomalies detected by the camera array with estimates of traversed distance enables quick relocation of areas of interest for follow up processes by divers or ROVs. The shape of the cable in the water column is estimated by plotting measurements of vehicle orientation and depth against the traversed distance estimates. A forward facing camera is used to identify buoyancy material on the riser cable to trigger the end of mission detachment sequence.

4. Traversal System

4.1. Attachment

The attachment jaws (Figure 4a) clamp onto riser cables between 160 mm and 210 mm in diameter. They are designed so a single jaw is sufficient to maintain the system's position on the cable under the largest expected environmental loads, without causing damage to the cable.

Loads on ARIS are due to waves, current and the submerged weight of the vehicle as shown in Figure 4b. The largest disturbance occurs where these forces are aligned and acting perpendicular to the direction of traversal since this creates a moment about the centre of the cable. The system is designed so that this moment can be withstood by the friction force at each jaw, which is a function of the gripping force. This scenario provides a conservative criteria since

in practice, the current loading component will generally act horizontally while the robot's net weight or buoyancy acts vertically.

For near water-surface operation, the wave and current induced force is calculated using Morison's equation (Morison et al., 1950),

$$F_M = \rho C_m V \dot{u} + 0.5 \rho C_d A u |u|, \quad (1)$$

where ρ is the density of seawater and u is the water particle velocity. C_m and C_d are the robot's inertial and drag coefficients, and V and A are its volume and projected area, respectively. The minimum frictional force required at each jaw-cable interface to prevent slip is found using rotational equilibrium about the cable centre as

$$F_F = \frac{h(F_M + W_W)}{4R}, \quad (2)$$

where the terms are defined in Figure 4b. The frictional force is a function of the normal force at each jaw-cable interface exerted by the linear actuator. The required gripping force, F_G from the actuator is,

$$F_G = \frac{h(F_M + W_W)}{4R\mu \cos \theta}, \quad (3)$$

where μ is the friction coefficient of the cable surface. We assume the robot is ballasted to be close to neutrally buoyant in seawater, as with most AUVs and inspection class ROVs that are trimmed to be slightly positively buoyant so that they can return to the surface in an emergency. The near neutral buoyancy minimises the disturbance of the robot on the riser cable, which is important as the shape of the cable is characterised during inspection, and it also reduces the required gripping force. We also assume the robot will operate in a similar environment to Hywind, where the maximum expected sea currents are 0.2 m.s^{-1} . The required gripping force is determined using the values in Table 2, which assume a moderate sea state and surface conditions (Morison et al., 1950). A 12 V electric linear actuator with a maximum force of 750 N can provide the required force (i.e., 491 N in Table 2) with a large safety factor.

The jaw is constructed of Aluminium 3003 sheet metal, where finite element analysis was performed to ensure sufficient strength. For the full-scale prototype for dry laboratory experiments, a material thickness of 2 mm can withstand a maximum stress of 76 MPa, giving a safety factor of 2.4 for the stress expected in the system. Off the shelf linear rails and bearings are used, and these are aligned with the linear actuator to efficiently transfer the load. A scissor mechanism between the jaws allows them to close symmetrically about their centre using just a single actuator. This keeps the outer surface of the riser cable in a consistent position relative to the robot. The scissor mechanism is

Table 2

Parameters used to calculate the required grip force.

Name	Symbol	Value	Unit
Seawater density	ρ	1025	kg.m ⁻³
Inertial coefficient	C_m	2	
Volume	V	0.0226	m ³
Particle velocity	u	0.792	m.s ⁻¹
Particle acceleration	\dot{u}	0.496	m.s ⁻²
Drag coefficient	C_d	1.3	
Projected area	A	0.052	m ²
Morison force	F_M	44.7	N
Lever arm	h	0.2	m
Weight in water	W_w	0.0	N
Cable radius	R	0.105	m
Cable friction coefficient	μ	0.057	
Jaw angle	θ	40	°
Actuator grip force	F_G	491	N

made of Aluminium 6082T6 flat bar, and is designed to withstand the maximum force from the linear actuator (i.e., 750 N) with a safety factor of 3.

A 25 mm thick layer of closed cell neoprene rubber is bonded to the jaw faces at the cable interface. This increases the frictional coefficient at the cable interface and evenly distributes pressure from the gripping force to avoid damaging the cable surface. The compliant material also allows barnacles and other small protrusions on the cable to be enveloped without affecting the gripping performance.

4.2. Drive

ARIS traverses along the cable using a single top-mounted linear actuator and two adjacent linear rails that act as guides to improve stability and motion under load. The linear actuator used for the drive motion is not required to exert as much force as the actuators used for the jaws, since it does not need to grip the cable, and a longer and faster stroke is desirable to maximise the inspection rate. A 12 V linear actuator with a 300 mm stroke length and 45 mm.s⁻¹ maximum stroke rate is used. This was chosen to minimise the number of drive cycles to complete an inspection, while ensuring that during the DE and DC (i.e., push and pull) phases of the drive cycle, the open jaws will not loose contact with a cable at its minimum bend radius of 2 m. Figure 5 illustrates the robot in its fully extended position on a section of cable with a 2 m radius of curvature. The maximum force the actuator can exert is 200 N, which is sufficient to overcome drag of the jaws during the push and pull phases of the drive.

Polyurethane rollers are fitted to the jaws, where these are mounted on rotational springs so that they fold away when the jaws clamp onto the cable. These maintain cable contact when the jaws are opened to maintain alignment with the cable during the DE and DC phases of the drive, while still being able to pass over barnacles and small obstacles. Rolling along the cable surface while exerting force minimises the risk of snagging or damaging the cable

275 surface. During the initial attachment to the cable, the rollers on the bottom of the jaws are connected to a pulley system
 276 that automatically pulls them out of the way when the jaws open near their widest range, but without obstructing the
 277 sprung roller function during operation when the jaws are in a narrower position. The key design variables for the
 278 sprung rollers are the lever arm length and spring stiffness. The force from the rollers normal to the cable surface, F_x ,
 279 originates from the stiffness, k in N.rad^{-1} , of the torsion springs at the pivot and varies with the arm length, L , and
 280 angular position, ϕ :

$$F_x = \frac{k\phi \sin \phi}{L} \quad (4)$$

281 A lever arm of 80 mm was chosen to maximise the normal force on the cable for a given stiffness, while making sure
 282 the roller components do not obstruct the view of the cable during inspection.

The rollers are oriented in a way that the moment they apply to the cable supports the alignment of the robot and cable when one of the jaws is released during the DE and DC phases of the drive cycle. The angular position of the roller varies as H in Figure 6 changes when a jaw is unclamped. The change in H can be calculated as,

$$\Delta H = \Delta y \sin \theta, \quad (5)$$

Substituting equation 5 into equation 4 gives the change in normal force on the cable from the roller as a function of Δy ,

$$\Delta F_x = \frac{k}{L} \cos^{-1} \left(\frac{\Delta y \sin \theta - r}{L} \right) \sqrt{1 - \left(\frac{\Delta y \sin \theta - r}{L} \right)^2}, \quad (6)$$

283 where the sign of Δy , shown in Figure 6, is positive when the centre line of the cable is further from the top frame than
 284 the centre of the jaws. The vertical and horizontal reaction forces on the system are given by the sin and cos components
 285 of F_x respectively. When one jaw is ungripped during a drive cycle, the springs act as passive restoring forces that
 286 stabilise the robot's alignment with respect to the cable under environmental loads or due to the robot's immersed
 287 weight, or buoyancy, if it is not perfectly neutrally buoyant. The parameters used in the design of this prototype are
 288 given in Table 3 and can be used to find the roller forces for a given Δy .

Table 3

Parameters used to calculate the roller forces on the cable in the prototype design.

Name	Symbol	Value	Unit
Stiffness	k	0.126	N.m.rad ⁻¹
Pivot arm length	L	80	mm
Angular position	θ	40	°
Roller radius	r	7.5	mm

5. Autonomous Behaviour

5.1. Control System Design

ARIS uses two low-cost on-board microcontrollers during operation. High level autonomous mission management, control, visual processing and data logging are achieved using a Raspberry Pi, which interfaces with the actuators and sensors of the system via a Arduino Mega (see Table 4).

Table 4

List of physical components that make up the control system.

Component	Quantity
Jaw actuator (750 N)	2
Drive actuator (300 mm stroke, 200 N)	1
Motor driver	3 (one per actuator)
Current sensor	3 (one per actuator)
Limit switch	2 (one per jaw actuator)
Ultrasonic sensor	2 (one per jaw actuator)
Camera	5 (one forward facing)
IMU	1
Linear potentiometer	1
Arduino Mega	1
Raspberry Pi	1

Figure 7 shows the autonomous mission workflow. The initial state of the robot is to have its jaws fully open and its drive actuator fully contracted. For attachment, it uses an ultrasonic sensor to measure the range to the cable, and when the cable is detected, the system grips the cable with both jaws as shown in the IA state in Figure 3. Successful attachment is judged by measuring the current of both jaw actuators, which increase when the jaws make contact and their contraction is resisted by the cable. Once attached, the robot goes through the drive cycle shown in Figure 3, repeating from FR to RG to traverse the cable while gathering inspection data. To achieve robust operation, the robot constantly monitors its sensors to identify three types of scenario. The first is a completion check, where the robot has either reached the buoys on the riser cable, the maximum mission time has elapsed, or reached a predefined depth limit that has been set. These all trigger detachment, where the robot fully opens its jaws to detach from the cable for recovery. In an underwater scenario this would also trigger a drop weight release or inflate a buoyancy engine to return to the surface. The second scenario is when the robot encounters an obstacle. Obstacles are detected by

305 monitoring the electrical current to the drive actuator, which increases when there is resistance to its motion. This
306 initiates a series of pass attempts to overcome the obstacle by widening of the obstructed jaw. If successful, the robot
307 continues its inspection, otherwise the obstacle is considered impassable and the robot detaches itself for recovery. The
308 final scenario is where the robot does not detect the cable using its ultrasonic sensor after initial attachment. In this
309 scenario, the robot assumes that it has partially or fully detached from the cable, and the robot opens its jaws to ensure
310 full detachment for recovery. An assumption is made that the robot has sufficient grip to not slip along the cable during
311 traversal, which is reasonable since this criteria is considered during jaw actuator selection.

312 **5.2. Intelligent Sensing**

313 This section describes three novel sensing methods developed to achieve the autonomous decision making in
314 Figure 7. Visual processing using the inspection camera array to aid motion estimation is described in section 6.3.
315 The first method determines where the riser cable is in relation to the robot, which is used to trigger initial attachment
316 and also to verify the robot has not become detached during traversal. This is achieved using ultrasonic sensors on the
317 jaws that measure the perpendicular distance between the top of the robot's frame and the cable surface. Once this
318 distance is within a preset threshold, the system now knows the cable is in range for the jaws to grip it. This check
319 is applied whenever the jaws are attempting to grip the cable, i.e., IA, and in the FG and RG jaw gripping phases of
320 Figure 3.

321 The second method determines the presence of obstacles by monitoring actuator currents. Since the current of
322 the linear actuators increase linearly with force, monitoring the current for each jaw during IA, FG and RG after
323 confirming cable presence (using the ultrasonic sensors), allows resistance from making contact with the cable to be
324 monitored. A current threshold can be determined based on a desired force from the actuator calibration. Advantages
325 of this simple force feedback approach are firstly that the cable diameter does not need to be known beforehand for
326 the robot to operate, and secondly that small variations in the surface will not affect the gripping strength, allowing for
327 robust performance. Figure 8 illustrates the expected electrical current profile during traversal. The next phase of the
328 drive sequence is triggered by the current to the active jaw actuator exceeding a predetermined threshold. The same
329 principle is applied on the drive actuator, where in this case, resistance indicates an obstacle in the direction of motion.
330 This triggers obstacle pass attempts, described in section 5.3.

331 The final method uses a forward-facing camera to detect buoyancy modules on the cable at the end of the catenary
332 runs illustrated in Figure 1. This indicates a successful end of mission. Visual processing based on the Hue, Saturation
333 and Value (HSV) of pixels in an image is used for buoy identification. Since the robot uses its own Light Emitting
334 Diodes (LEDs) to illuminate the scene at close proximity (1 m range), and the contribution of ambient light beyond
335 ~50 m water depth is minimal, a high degree of repeatability can be expected as long as the colour of the buoyancy

material is known. The relative configuration of the robot attached to the cable is highly constrained. This means that for a fixed camera field of view, the area of the scene occupied by the buoy can be used as a distance to buoy proxy. A threshold for a minimum number of pixels identified as belonging to a buoy based on their HSV parameters is used to trigger robot detachment for the end of mission. For the camera opening angle used in this work, a threshold of 50 % of the camera frame detected as yellow (corresponding to the usual colour of buoyancy sections) is used. The large threshold is chosen for robustness against misclassification of the riser cable and particles in the water column as belonging to a buoy.

5.3. Obstacle Avoidance

Although large obstacles can be detected using the forward facing camera, smaller obstacles can be challenging to robustly recognise. In these situations, resistance to motion of the drive actuator, causing an increase in actuator current, is a robust indicator of obstacle encounter. In these situations, the robot triggers a pass attempt, where it widens the jaw that encountered the obstacle, i.e., front jaw during DE and rear jaw during DC of Figure 3, and attempts the same drive manoeuvre again. Success is determined by monitoring the current drawn by the drive actuator and the range limit switch of each jaw actuator. Jaw widening followed by driving is repeated until either the obstacle is overcome (i.e., DE or DC completion with current not exceeding the threshold) or the jaw is at its widest (hitting the limit switch) and still fails to pass the obstacle (shown in Figure 9). If the obstacle is passed the system continues its traversal. If the obstacle cannot be passed, the robot ends the mission and detaches from the cable for recovery.

6. Inspection System

6.1. Cable Damage Detection

Four LED illuminated cameras are mounted on ARIS concentrically to the cable at 90° on the rear jaw frame to inspect the full 360° of the cable surface. Figure 10 shows the design of the cameras that are arranged to detect damage on the cable surface and also help estimate motion of the system using optical flow. The camera vertical field of view of 62° allows the observations to overlap on the maximum diameter of cable targeted (i.e., 210 mm) so that no detectable anomalies are missed, as shown in Figure 10. The figure shows the setup for a pair of cameras on one side of the rear jaw, where a mirrored setup exists on the opposite side of the jaw. The location of the cameras is chosen to maintain a continuous view of the cable, while minimising the overall size of the robot's frame. In this configuration, the axial field of view at the nearest part of the cable is 104 mm with images acquired continuously at 30 fps. During each drive cycle, the drive actuator moves at $\sim 26 \text{ mm.s}^{-1}$. By pausing the drive actuator every 2 s for a short interval of 0.1 s, it is possible to ensure motion blur free images are captured with a minimum overlap of $\sim 50\%$ between consecutive stills. These can be used for crack detection and mosaicking. The cameras achieve a minimum pixel resolution for all

cables within the target diameter range of 0.2 mm in both the along and across cable directions, which is adequate for detecting cracks >0.5 mm wide. For operation in water, these field of view and resolution requirements need to be met after accounting for the difference in refractive index between air and water (Bodenmann et al., 2017).

Damage to the cable surface is detected off-line using visual processing. A Canny edge detection algorithm (Canny, 1986) implemented using the OpenCV library is used to detect cracks as more than 0.5 mm with tolerance for water turbidity. The algorithm returns a positive crack detection if more than 200 key points are detected in each 0.3 MPx image frame. This limit was found experimentally to provide reliable performance. Lower values are more prone to noise, detecting LED reflections on the cable and from particulates, and larger values are liable to miss smaller defects on the cable surface. Noise reduction is achieved using the functions listed in Table 5.

Table 5
Functions of the post-processing filters.

Filter	Function
bilateralFilter	Noise removal while keeping edges sharp
Dilate	Joining broken parts of an object after noise removal
medianBlur	Smoothing the image
logtransform	Image enhancement, expand dark pixels of the image as compared to higher pixel values
morphologyEx	Closing small holes inside the foreground objects, or small black points on the object
Aperaturesize	Size for the Sobel operator in Canny edge detection, which emphasises edges

6.2. Riser Shape Monitoring

The catenary shape can be estimated using the robot's depth, measured by a pressure sensor, and its orientation (assumed tangential to the cable), as measured by an IMU. The orientation of the robot measured using an IMU is expressed as quaternions to avoid singularities, or Gimbal lock when describing the robot's orientation at high elevation angles (Kuipers, 2002; Thornton et al., 2007). These can be combined with the estimated position along the cable (see Section 6.3). The global shape is estimated using a cubic regression of the estimated position, depth and orientation measurements made at each drive cycle, i.e., at ~300 mm intervals. The resolution of these measurements is high compared to the minimum bend radius and expected length of the cable, which are 2 m and 125 m respectively at Hywind.. The cable's radius of curvature is estimated using Equation 7 from which checks can be made against the

minimum bend radius, and assessments of the likely fatigue rate can be made.

$$R = \frac{\left[1 + \left(\frac{dy}{dx}\right)^2\right]^{\frac{3}{2}}}{\left(\frac{d^2y}{dx^2}\right)}, \quad (7)$$

where for riser cables at Hywind $R < 2$ m is of concern.

6.3. Position Estimation

The system generates position estimates to locate the inspection outputs and allow faults to be revisited. Global Navigation Satellite Services (GNSS) such as the Global Positioning System (GPS) cannot be used due to the strong absorption of radio waves in water. Acoustic positioning systems can be used, but are expensive and require additional local infrastructure. Also, multi-pass reflections of acoustic signals from nearby infrastructure are expected to degrade performance reliability for this application. Physical landmarks can be used (Bonnin-Pascual and Ortiz, 2019), but these also require modification of the operating environment, which would add significant complexity to robot deployment. Odometry measures the relative motion over short distances, or the velocity, of a mobile platform. These can be integrated to estimate the cumulative distance travelled relative to some known location along the trajectory. Limitations of odometry are firstly that some reference position along the trajectory needs to be known in order to locate observations, and secondly, that odometry suffers from drift errors when measurements are integrated (Ferrera et al., 2019).

For the reference location, we assume that the deployment system will provide an initial attachment position that will be available for position estimation. Furthermore, for missions that reach the buoys at the end of the trajectory, the known position of these can provide a second reference point that can be used to correct for any error accumulation during traversal. In order to minimise the drift error that accumulates, which may be problematic in situations where the robot detaches before reaching the buoys, the system uses multiple sources of odometry information, and uses a KF (Bonnin-Pascual and Ortiz, 2019) to fuse these and estimate the distance travelled along the cable axis.

The first source of odometry information is a linear potentiometer (SoftPot 400 mm) attached to actuated drive mechanism between the front and rear jaws. This measures the distance between the jaws, where summing the extension during the DE phase of the drive cycle (Figure 3) provides an estimate of cumulative distance travelled, assuming that the jaws do not slip on the cable (see previous discussion in section 4.1). The second source of information is the IMU acceleration data used for cable shape and motion monitoring. For this, we assume the robot is oriented along the cable's major axis during its drive phase, so that a single axis of acceleration data can be integrated twice to estimate the position change after accounting for acceleration due to gravity for non-zero elevations. A low-pass filter is used to remove noise from the signal, and the intermediate velocity is capped so that it does not exceed the maximum velocity

of the drive actuator. The third source of information is visual odometry using the images taken by the 360° field inspection camera array. The visual odometry system assumes that the pixel intensities of an object do not change between consecutive frames and that neighbouring pixels have similar motion. The algorithm implemented using the OpenCV library in Python first detects a number of corner features in an initial frame using the Harris Corner Detection algorithm (Harris and Stephens, 1988), using a modified Shi-Tomasi reward (Shi and Tomasi, 1994). Once the corner features are detected, the Lucas-Kanade method is used to track these over a known time period in a subsequent image frame (Lucas and Kanade, 1981). For all successfully matched corner features between the image frames, the average magnitude of motion is calculated in pixels, which is converted to a true distance based on the camera field of view, the range to the cable surface and its diameter. This cable diameter is determined from the jaw opening distance when the cable is gripped, and the range to the cable is determined based on the cable geometry. An advantage of using visual odometry is that it does not rely on the assumption that the jaws do not slip. Figure 11 shows an example of corner features that have been detected and tracked between multiple image frames in simulation. The visual odometry outputs can be used to detect if the robot slips during operation, where a large discrepancy between the visual odometry outputs and the linear potentiometer and accelerometer based odometry outputs, which in turn would cause a large degree of uncertainty in the position estimates of the KF described next.

Estimating cumulative position based on the measurements of relative motion along a single axis is a linear problem. Therefore, a KF can be used to combine the measurements of the three odometry sources by modelling the uncertainty of each odometry sensor with a normal distribution as follows (Kalman, 1960):

- Initialise - Variables and counters are defined. Position estimates are given by x , position variance p , and process noise variance is q , which is the uncertainty in the dynamic model used for predictions. Counters for the timestep and sensor number are i and n respectively.
- Predict - At time i , a constant velocity model is used to predict the new position of the system after time interval Δt . The uncertainty is updated due to the introduction of process noise. The subscript $(i, i - 1)$ represents an unfiltered prediction at time i based on the previous value of a quantity at time $(i - 1)$.

$$x_{i,i-1} = x_{i-1,i-1} + \Delta t \dot{x} \quad (8)$$

$$p_{i,i-1} = p_{i-1,i-1} + q \quad (9)$$

- Measure - Readings are taken from each sensor, z_n , and added to the previous position estimate to estimate the total distance travelled:

$$z_n = z_n + x_{i-1,i-1} \quad (10)$$

- Update - The Kalman gain, K , is calculated as a function of the sensor's variance, r_n , and the prediction variance. The Kalman gain is used to update position estimates depending on prediction and measurement uncertainties, and a variance is calculated for the corrected estimate. The update step is repeated for each sensors' observation (Willner et al., 1976).

$$K_n = \frac{p_{i,i-1}}{p_{i,i-1} + r_n} \quad (11)$$

$$x_{i,i} = x_{i,i} + K_n(z_n - x_{i,i}) \quad (12)$$

$$p_{i,i} = (1 - K_n)p_{i,i} \quad (13)$$

- Output - Following iteration of the update stage for each sensor reading, $x_{i,i}$ is the most probable position of the system at time i .

Figure 12 shows the results of a numerical simulation of the system moving at a velocity of 45 mm.s^{-1} along a cable for 3000 s, traversing a total distance of 135 m. The uncertainty of the potentiometer, IMU and optical flow measurements are modelled as 10 mm, 40 mm and 30 mm, respectively. For the potentiometer and optical flow, each sensor's variance was determined experimentally based on its response to a drive cycle, where the actual distance travelled was measured externally to provide ground truth. For the IMU, uncertainty estimates were based on manufacturer specifications. The prediction uncertainty for the constant velocity model is set to 5 mm.s^{-1} , where this provides sufficient uncertainty to accommodate expected variability in the drive cycle velocity during typical cable traversal. The simple averaging approach causes a large accumulation of error in position, but the KF models the relative uncertainty of each measurement type, resulting in a smaller error under the simulated condition.

7. Experimental Verification

A series of lab-based experiments are performed using a full scale prototype of ARIS. The riser cable was modelled using a 3 m section of 160 mm diameter pipe and all experiments were conducted in air. Due to limitations of the experimental setup, a simulator was also used to validate the proposed method for estimating the shape of the cable. The results of the experiments are summarised in Table 6, with details of each experiment in the following subsections.

Table 6

Summary of experimental results.

Attachment and grip	
Cable diameters	160 to 210 mm
Attachment position tol.	± 62 mm
Max. grip force	~ 650 N
Max. pressure on cable	9 kPa
Traversal	
Rate along cable length	$\sim 24 \text{ m.h}^{-1}$
Drive cycle distance	300 mm
Max. cable bend radius	2 m
Traversable obstructions	15 mm protrusion (compliant jaw material) 50 mm protrusion (autonomous jaw widening)
Inspection	
Cable surface imaging	360° field of view at 0.2 mm resolution
Min. detectable crack	0.5 mm
Position accuracy	3 % of distance travelled along cable
Shape monitoring	Cable gradient within 2 % of actual orientation
Autonomous behaviour	
Attachment	Gripping of cable using ultra-sonic range sensors
Obstacle avoidance	Actuator current sensing and jaw widening
Buoyancy block detection	Forward looking camera and image processing

7.1. Attachment and Traversal Experiments

7.1.1. Attachment

The initial attachment of the system needs to overcome uncertainty in the position of the robot with respect to the cable. Based on the literature, we assume a transverse positioning accuracy of ± 50 mm that needs to be overcome by the autonomous attachment system (i.e., $D=50$ mm in Figure 13). During the experiment, the robot was lowered over the cable model using a crane. Figure 13 shows the vertical offset from the cable, V , which is continually monitored using an ultrasonic sensor situated in line with the bottom of the jaw frame. The jaws are triggered to grip when $V < 200$ mm. The lateral offset from the centreline that can be accommodated is determined by the clearance between the jaws when fully open and the gripping target. This gives a maximum tolerance of $D=62$ mm for a cable diameter of 210 mm (the largest diameter of cable targeted in this work), where the self-centring mechanism is able to correct for any positioning errors up to this value. This tolerance increases for smaller cable diameters.

460 **7.1.2. Grip Force and Pressure**

461 The system is required to exert high forces on the cable while keeping the pressure at its interface below 6.9 MPa to
462 avoid damage to the cable sheath. The forces applied by the jaws for various current limits were measured by clamping
463 a load cell between spacers as shown in Figure 14a. To find the pressure at a given force, the contact area was measured
464 from the imprint formed by the compliant pad to determine the jaw's contact area.

465 The results in Figure 14c show a linear relationship between the current and force generated, with a maximum grip
466 force of ~ 650 N achieved, which is $1.3\times$ the minimum requirement to avoid slipping for the expected environmental
467 loads and friction coefficient. The maximum force exerted corresponds to a pressure of 9 kPa on the cable surface,
468 which is $\sim 1/800$ of the 6.9 MPa damage limit for the cable sheathing material.

469 **7.1.3. Gripping and Traversal Over Small Obstacles**

470 Small obstacles on the cable such as barnacles should not obstruct the attachment or traversal of the system. In
471 particular, it is important that small protrusions do not cause the gripping force to exceed the damage threshold of the
472 cable sheath. A small obstacle is simulated by attaching a 15 mm protrusion to the pipe cross section. The jaws are
473 attached on top of the protruding object and a drive cycle is carried out to confirm that traversal is possible and ensure
474 the spring loaded rollers can pass over the obstacle.

475 Figure 15a shows the compliant jaw pad forming an envelope around the protrusion and maintaining a large contact
476 area with the pipe. Figure 15b shows the roller passing over the obstacle. This confirms that the system is capable of
477 operating in the presence of solid marine growth such as barnacles on the target cable without risk of damaging the
478 cable or compromising an inspection.

479 **7.2. Autonomy Testing**

480 **7.2.1. Obstacle Avoidance**

481 ARIS attempts to pass obstacles that obstruct standard DE and DC manoeuvres but are physically passable (i.e.,
482 protrude less than the jaw clearance at their maximum opening) without compromising the robot's safety. This behaviour
483 is needed as during standard operations, the distance the jaws open is kept as small as possible since righting forces
484 provided by the spring mounted rollers decrease with increased clearance from the cable surface, reducing drive motion
485 stability.

486 The results of experiments performed with an obstacle protruding 50 mm from the surface of the cable model in the
487 path being traversed by the robot are shown in Figure 16b and 16c. These compare the currents measured on the robot's
488 actuators during a standard drive cycle to when the robot encounters an obstacle and attempts to pass it according to the
489 obstacle avoidance workflow in Figure 9. In the plots, negative current indicates opening of the jaws and contraction of
490 the drive actuator. During normal operation, the magnitude of the drive actuator current remains around 1.0 A, which

491 is lower than the 1.2 A magnitude threshold set for obstacle detection (shown as green dotted lines). For the obstacle
492 avoidance experiment, the drive current increases as the drive actuator's motion (DE) is resisted by the obstacle. When
493 the current exceeds the 1.2 A threshold set for obstacle detection, the obstacle is detected and the drive actuator is
494 contracted by a small amount (denoted DC'). The obstructed front jaw is opened by a small amount (denoted FR'),
495 before extending the drive actuator (DE). On the second pass attempt, the front jaw successfully passes the obstacle
496 with the drive actuator current remaining below the set threshold. Once fully extended, the front jaw grips the cable
497 model (FG) to continue the drive cycle.

498 **7.2.2. Buoyancy Module Detection**

499 Detection of buoyancy material on the cable signals the end of a mission as these are large and cannot be passed.
500 Experiments were performed to verify buoyancy detection using the proposed visual processing method (see Figure
501 17a). The buoyancy module was modelled using yellow material that covered a large enough area to trigger detection.
502 Detection is triggered when 50 % of the forward camera image matches the HSV parameters tuned to identify buoyancy
503 at the end of a complete drive cycle. For the purpose of this experiment, detection of the buoyancy was programmed to
504 terminate traversal, whereas in actual operation, buoy detection would trigger detachment from the cable for recovery.

505 During the experiment, the system completes two drive cycles, where after the first cycle, less than 50 % of the
506 image is classified as belonging to a buoy. As a result, the robot completes another drive cycle, after which more than
507 50 % of the image is classified as belonging to a buoy, triggering the end of mission. Since the distance traversed
508 during each cycle is approximately 300 mm, waiting until the end of a drive cycle to check for the buoyancy modules
509 does not pose a collision threat. Running the detection algorithm takes approximately 0.1 s per image, which does not
510 significantly delay the next drive cycle.

511 **7.3. Inspection Experiments**

512 **7.3.1. Crack Detection**

513 Experiments were performed to verify automated detection of damage to the cable's outer sheath that are wider
514 than 0.5 mm. Processing is done offline to generate inspection products together with their position estimates since the
515 robot does not need to identify cracks in realtime for its operation.

516 To investigate the performance of the crack detection, simulated crack patterns with a thickness of 3 mm were
517 drawn on the cable model and inspection images were gathered using the 360° inspection camera array as the robot
518 traversed over the simulated cracks. Figure 18, shows the results of offline crack detection, where it can be seen that
519 robust crack detection can be achieved. The bright region of the image is reflection of the LEDs from the pipe used
520 to model the cable surface. The crack detection is not affected by this since the gradual reduction in brightness in
521 the reflected pattern does not trigger an edge detection. It should be noted that the actual cable surface is expected to

522 be less reflective than the model used in this experiment. In an underwater environment, turbidity is likely to cause
523 scattered reflections that can degrade the performance of crack detection. However, the degradation would be similar
524 to the levels experienced by divers and in images obtained using ROVs that are currently used for riser cable surveys,
525 and so is not a limiting factor for the proposed inspection method.

526 **7.3.2. Shape Monitoring**

527 Verification of the cable shape mapping was carried out using a computational simulation environment at full-
528 scale, and at a smaller scale using the prototype on the experimental rig. For the smaller scale physical experiment,
529 the prototype performs two drive cycles on an inclined cable model while measuring the orientation of the robot. The
530 results generated assume that the robot remains aligned with the major axis of the cable, and travels in the direction
531 along its major axis, where both assumption are reasonable given the design of the platform. The inclined experiment
532 was conducted with the cable model inclined at 22° to horizontal. The orientation measured by the IMU is processed
533 as described in section 6.2 and the results are compared to the actual cable shape.

534 The difference between the estimated and actual cable inclination (see Figure 19a) is small, where a linear regression
535 of the shape estimate has a gradient within 2 % of the actual cable inclination. This results in a 12 mm deviation over
536 a 600 m length of cable, which is considered acceptable, in particular given that in the ocean depth sensor data will
537 also be available to improve the accuracy of the shape information. It should be noted that the experiment is for a rigid
538 section of cable, curved sections with a bend radius of >2 m are expected to be geometrically traversable with the
539 maximum extended length of the robot, where the elevation and heading angles of the curved sections will be sampled
540 at the resolution of a drive cycle.

541 A simulation for a longer section of cable is performed to validate the method for determining cable bend radii.
542 The IMU and depth sensors were simulated together with the robot and a section of cable using the ROS Gazebo
543 environment (Koenig and Howard, 2004). The simulation models a simplified version of ARIS, which traverses a
544 static cable that has a known shape for method verification. The IMU recordings simulated as ARIS traverses a curved
545 cable section are run through the cable shape monitoring method described in section 6.2. Figure 19b shows the cable
546 shape estimated using the Gazebo acquired data. The small scale experimental results and simulation outputs show that
547 the shape can be determined using the proposed methods as long as accurate estimates of the distance traversed along
548 the cable axis can be obtained. Although the method can work regardless of the relative angle of the robot about the
549 cable centreline, having a positive righting moment so that the robot's jaws have their opening vertically downwards is
550 practical for deployment and recovery purposes, and maintaining a fixed relative angle about the cable centreline also
551 simplifies the analysis for determining cable shape.

7.3.3. Position Estimation

The traversed distance needs to be estimated with sufficient accuracy relative to a known location in the data to allow follow-up maintenance and intervention tasks to efficiently relocate areas identified by the inspection. Experiments are performed using the KF to combine visual odometry with the measurements of the linear potentiometer. The acceleration values of the IMU were not used due to the high level of noise in their measurements compared to the visual odometry and potentiometer measurements. Experiments with two drive cycles traversed 496 mm in 75 s, giving an inspection rate of $\sim 24 \text{ m.h}^{-1}$, meeting the initial design requirement set out in Table 1. The potentiometer measurements have a resolution of 1.76 mm with $\pm 10 \text{ mm}$ uncertainty. The visual odometry tracked 15 features that were refreshed every 55 frames to ensure the features remained in frame for effective tracking. The measurement uncertainty has a value of $\pm 30 \text{ mm}$.

Figure 20a shows the output of the KF combining the predictions and measurements from both sensors to estimate the position of the system, where the true position of the system was measured externally to verify the results. The absolute error values shown in Figure 20b show that the KF is effective for reducing the estimated position's error compared to summing and averaging of sensor inputs.

Although the distance traversed in this experiment is short, the position estimate is within 3 % of the distance travelled. When extrapolated over the traversed distance of a 125 m cable section, this translates to an error of $< 4 \text{ m}$, which is sufficient for divers or ROVs to relocate any observations identified in the inspection data. Further improvements can be expected by using higher resolution cameras, accelerometers and potentiometers. Nonetheless, the results demonstrate the feasibility of odometry-based localisation of observations made during riser cable inspection.

8. Conclusions and Future Work

We have developed hardware concepts, control, sensing and data processing methods to enable autonomous mobile robotic inspection of riser cables, as used by floating offshore wind facilities. The robot, referred to as ARIS (Autonomous Riser Inspection System), is untethered, and operates without human supervision. ARIS uses a dual jaw, clamp and push drive mechanism driven by three linear actuators to attach itself to a cable of diameter 160 mm to 210 mm with a bend radius $> 2 \text{ m}$, and traverse it while gathering inspection data. A full-scale prototype measuring 600 mm in length when contracted, 650 mm wide and 400 mm high, and weighing 23.2 kg in air has been developed. Experiments performed prove the proposed solutions are feasible methods to inspect riser cables in combination with established technology for waterproofing, hardware ruggedisation, deployment, in water localisation and recovery. The novel developments in this work have established that:

- The proposed dual jaw, clamp and push drive mechanism demonstrates traversal at a rate of $\sim 24 \text{ m.h}^{-1}$ while providing sufficient grip force of $\sim 650 \text{ N}$ to withstand disturbances due to currents of 0.2 m.s^{-1} and moderate surface wave conditions. The design minimises the pressure applied to the cable surface to $\sim 1/800$ of its damage threshold by using compliant gripping material on the jaw interface. The compliant rubber also allows the cable to be gripped securely in the presence of small obstructions on the cable surface. Spring loaded rollers on the jaw mechanism maintain contact with the cable at all stages during the traversal drive phase, generate a righting force to centralise the robot on the cable section in the presence of disturbances and non-neutral buoyancy. The dry laboratory experiments demonstrate the feasibility of inspecting a dynamic riser cable in a few hours.
- The position of the robot along the length of the cable can be determined to within 3 % of distance travelled by combining the measurements of a linear potentiometer between the front and back jaws of the robot, and visual odometry using optical flow information from an array of four cameras that view the 360° surface of the cable. The measurements from these sensors are combined using a Kalman filter, and additional sources of input (e.g., acceleration measurements) can also be incorporated. Provided either the start or the end location of the inspection run is known, this allows the condition observations to be located to better than 4 m for a 125 m long catenary section, allowing for efficient relocation by divers or ROVs as necessary.
- Small obstacles attached to the cable can be automatically detected and pass attempts made by monitoring actuator currents and responding accordingly. The method detects obstructions to drive actuator extension or contraction, triggering wider opening of the obstructed jaws until the obstruction can be passed or until the robot determines the obstacle to be non-passable. Tests conducted over a 50 mm high protrusion from the cable surface demonstrate successful detection and pass attempts, verifying the performance of the method. A method has also been developed to detect large buoy modules that are attached to the riser cables. The method uses visual feedback from a forward facing camera to identify buoys and safely end a mission. The two methods described allow the robot to autonomously and safely navigate its environment without relying on a human operator.
- A method to automatically detect a cable and grip it has been developed and successfully demonstrated. The method uses ultrasonic range sensors to measure when the device is brought over a cable, and the jaw design allows for attachment with lateral position uncertainties of up to 62 mm when gripping a cable of diameter 210 mm. The robot detects whether it has successfully gripped the cable by monitoring the electrical current supplying the jaw actuators, allowing the robot to grip cables with diameters of between 160 mm and 210 mm without prior knowledge of cable geometry. The positioning needed to bring the robot close enough for this method to work is considered achievable based on the literature for accurate relative positioning of AUVs and

ROVs. The same ultrasonic sensor allows the robot to detect whether it has become fully or partially detached from the cable, in which case the robot prepares itself for recovery.

- Novel sensing methods to detect the shape and condition of the cable surface have been developed and experimentally demonstrated. Shape is measured using the orientation of the robot as it traverses the length of the cable, where we assume that the robot remains aligned parallel to the cable's central axis. This gives shape information with a resolution of ~ 300 mm, which is the stroke length of the robot's drive cycle. Experiments on an inclined cable model achieve an accuracy within 2 % of the actual incline, where the use of depth sensors could further improve the description of cable shape. The condition of the full circumference and length of the cable is inspected using an array of four cameras that view the entire length of the cable surface at a resolution of 0.2 mm. Automatic crack detection algorithms have been demonstrated to reliably identify surface defects that are wider than 0.5 mm using the measurements of this system.

The concepts for sensing and autonomous behaviour demonstrated are applicable to underwater use with appropriate marinisation. For use in the field, the use of brush or acoustic surface cleaning methods in combination with the demonstrated concepts should be explored to improve friction between the robot and the inspection target, and also remove bio-fouling that may obstruct the view of the cable surface during visual inspection. The dry experiments carried out in this work demonstrate sufficient grip and traversal performance under the static forces and moments expected during subsea inspection. However, riser cable dynamics cover a wide range of frequencies, including low tension excitation from floating platform motion and environmental forces (Pinto, 1995) and vortex induced vibrations of the risers themselves (Tri, 2005). Investigations of performance under dynamic conditions are recommended to take place in water due to the strong influence of the robot's added mass at higher frequencies.

CRediT authorship contribution statement

Christopher Gotts: Conceptualization, Prototype development, Experiments, Data analysis, Writeup. **Benjamin Hall:** Conceptualization, Prototype development, Experiments, Simulation, Data analysis, Writeup. **Oliver Beaumont:** Conceptualization, Prototype development, Experiments, Data analysis. **Ziyang Chen:** Conceptualization, Prototype development, Visual processing, Experiments, Data analysis. **William Cleaver:** Conceptualization, Prototype development, Experiments, Data analysis. **James England:** Conceptualization, Prototype development, Experiments, Data analysis. **David White:** Conceptualization, Project Supervision, Writeup. **Blair Thornton:** Conceptualization, Project Supervision, Writeup.

9. Acknowledgements

The authors thank the EDMC workshop of the University of Southampton for manufacturing the components for the prototype ARIS system developed in this paper. We also thank Harvey Skinner for his assistance in preparing the laboratory experiments in this work, JDR Cable Systems for providing valuable insights into riser cable inspection, and IGUS for their support providing components for the prototype ARIS.

References

- , 2005. Experimental investigation of vortex-induced vibration of long marine risers. *J. of Fluids and Struct.* 21, 335–361.
- Albitar, H., Dandan, K., Ananiev, A., Kalaykov, I., 2016. Underwater robotics: Surface cleaning technics, adhesion and locomotion systems. *Int. J. of Adv. Robot. Syst.* 13, 7. doi:10.5772/62060.
- BladeBUG, 2021. Bladebug: Advanced robotics for turbine maintenance. <https://www.bladebug.co.uk/>. (accessed 19 August 2021).
- Bodenmann, A., Thornton, B., Ura, T., 2017. Generation of High-resolution Three-dimensional Reconstructions of the Seafloor in Color using a Single Camera and Structured Light: Generation of High-Resolution. *J. of F. Robot.* 34, 833–851.
- Boenisch, A., 2015. Inspection Approaches and Experience for Inspecting Challenging Subsea Assets. Technical Report. Innospection. URL: https://www.subseauk.com/documents/presentations/andreas_boenisch_-_innospection.pdf.
- Bonnin-Pascual, F., Ortiz, A., 2019. On the use of robots and vision technologies for the inspection of vessels: A survey on recent advances. *Ocean Eng.* 190, 106420. doi:10.1016/j.oceaneng.2019.106420.
- Campos, D.F., Matos, A., Pinto, A.M., 2021. Multi-domain inspection of offshore wind farms using an autonomous surface vehicle. *SN Appl. Sci.* 3, 455. doi:10.1007/s42452-021-04451-5.
- Canny, J., 1986. A computational approach to edge detection. *IEEE Trans. on Pattern Anal. and Mach. Intell.* 6, 679–678.
- Dinmohammadi, F., Flynn, D., Bailey, C., Pecht, M., Yin, C., Rajaguru, P., Robu, V., 2019. Predicting damage and life expectancy of subsea power cables in offshore renewable energy applications. *IEEE Access* 7, 54658 – 54669. doi:10.1109/ACCESS.2019.2911260.
- Eldøy, S., 2017. Hywind Scotland Pilot Park Project Plan for Construction Activities 2017. Technical Report. Statoil. URL: <http://marine.gov.scot/sites/default/files/00516548.pdf>.
- Ferrera, M., Moras, J., Trouvé-Peloux, P., Creuze, V., 2019. Real-time monocular visual odometry for turbid and dynamic underwater environments. *Sensors* 19, 687. doi:10.3390/s19030687.
- Global Monitoring and Forecasting Center, 2021. Atlantic - european north west shelf - ocean physics analysis and forecast. https://resource.s.marine.copernicus.eu/?option=com_csw&view=details&product_id=NORTHWESTSHELF_ANALYSIS_FORECAST_PHY_004_013&pk_vid=f721a10624699cd61629883620fb3a43. (accessed 25 August 2021).
- Hachicha, S., Zaoui, C., Dallagi, H., Nejim, S., Maalej, A., 2019. Innovative design of an underwater cleaning robot with a two arm manipulator for hull cleaning. *Ocean Eng.* 181, 303–313. doi:10.1016/j.oceaneng.2019.03.044.
- Harris, C., Stephens, M., 1988. A combined corner and edge detector, in: *Proc. of Fourth Alvey Vis. Conf.*, pp. 147–151.
- IRENA, 2021. Offshore renewables: An action agenda for deployment. Technical Report. International Renewable Energy Agency. URL: <https://www.irena.org/publications/2021/Jul/Offshore-Renewables-An-Action-Agenda-for-Deployment>.
- Kalman, R.E., 1960. A new approach to linear filtering and prediction problems. *ASME. J. Basic Eng.* 82, 35–45. doi:10.1115/1.3662552.
- Kaur, A., Ma, B., Corsar, M., Sattar, T., L., C.A., Forrest, P., Nicholson, I., 2018. Risersure: Automated deployment of digital radiography for subsea inspection of flexible risers, in: *2018 IEEE 23rd Int. Conf. on Emerg. Technol. and Fact. Autom. (ETFA)*, pp. 736–742. doi:10.1109/ETFA.2

018.8502476.

Kimball, M., Sain, A., Gmerek, A., Collins, P., Wheatley, A., Shah, K., Liu, J., Dissanayake, M., Carroll, J., Plastropolous, A., Karfakis, P., Virk, G.S., Sattar, T., 2018. Mooring chain climbing robot for ndt inspection applications, in: The 21st Int. Conf. on Climbing and Walk. Robot. and Support Technol. for Mob. Mach. (CLAWAR 2018), pp. 339–347. URL: <https://revistas.utp.ac.pa/index.php/memoutp/article/view/1986>.

Koenig, N., Howard, A., 2004. Design and use paradigms for gazebo, an open-source multi-robot simulator, in: 2004 IEEE/RSJ Int. Conf. on Intell. Robot. and Syst. (IROS) (IEEE Cat. No.04CH37566), pp. 2149–2154 vol.3. doi:10.1109/IROS.2004.1389727.

Kuipers, J.B., 2002. Quaternions and Rotation Sequences : A Primer with Applications to Orbits, Aerospace and Virtual Reality. Princet. Univ. Press, Princeton, New Jersey.

Lucas, B.D., Kanade, T., 1981. An iterative image registration technique with an application to stereo vision (darpa), in: Proc. of DARPA Image Underst. Workshop (IUW '81), pp. 121 – 130.

Matsuda, T., Maki, T., Masuda, K., Sakamaki, T., 2019. Resident autonomous underwater vehicle: Underwater system for prolonged and continuous monitoring based at a seafloor station. Robot. and Auton. Syst. 120, 103231. doi:10.1016/j.robot.2019.07.001.

MatWeb, 2021. Borealis borstar® he6063 natural bimodal hd polyethylene compound for jacketing of communication and power cables. <http://www.matweb.com/search/DataSheet.aspx?MatGUID=77b1c3eaa5414e0f8e34f86a9bd92e4fZckck=1>. (accessed 05 August 2021).

McKeever, P., Young, D., 2020. Dynamic cabling - the challenges unique to fow, in: Virtual Wind 3. URL: <https://youtu.be/05nkQadjguc?t=10206>.

Morison, J.R., O'Brien, M.P., Johnson, J.W., Schaaf, S.A., 1950. The force exerted by surface waves on piles. Pet. Trans., AIME 189, 149–154. doi:10.2118/950149-G.

Pinto, W.T., 1995. The On the Dynamics of Low Tension Marine Cables. Ph.D. thesis. Univ. Coll. Lond.

Proskovics, R., 2017. An Introduction to Risk in Floating Wind. Technical Report. ORE Catapult. URL: <https://ore.catapult.org.uk/ap/p/uploads/2017/12/An-Introduction-to-Risk-in-Floating-Wind--Roberts-Proskovics--AP-0014.pdf>.

Rentschler, M.U.T., Adam, F., Chainho, P., 2019. Design optimization of dynamic inter-array cable systems for floating offshore wind turbines. Renew. and Sustain. Energy Rev. 111, 622 – 635. doi:10.1016/j.rser.2019.05.024.

Rolfe, C., Thornton, B., Massot-Campos, M., 2020. Development of a passively pre-tensioned buoyancy engine for fail-safe underwater vehicle operation, in: IEEE/OES Autonomous Underwater Vehicles Symposium (AUV), pp. 1–6. doi:10.1109/AUV50043.2020.9267914.

Santos, M.F., Brito, M.O., Neves, C., Menegaldo, L.L., 2013. Development of an underwater riser inspection robot. Ind. Robot: An Int. J. 40, 402–411. doi:10.1108/01439911311320895.

Shi, J., Tomasi, 1994. Good features to track, in: Proc. of IEEE Conf. on Comput. Vis. and Pattern Recognit., pp. 593–600. doi:10.1109/CVPR.1994.323794.

Singh, P., Ananthasuresh, G.K., 2013. A compact and compliant external pipe-crawling robot. IEEE Trans. on Robot. 29, 251–260. doi:10.1109/TRO.2012.2214560.

Song, C., Cui, W., 2020. Review of underwater ship hull cleaning technologies. J. Marine. Sci. Appl. 19, 415–429.

Thornton, B., 2020. Sizing drop weights for deep diving submersibles taking into account nonuniform seawater density profiles. IEEE J. of Ocean. Eng. 45, 979–989. doi:10.1109/OJE.2019.2898070.

Thornton, B., Bodenmann, A., Pizarro, O., Williams, S.B., Friedman, A., Nakajima, R., Takai, K., Motoki, K., Watsuji, T., Hirayama, H., Matsui, Y., Watanabe, H., Ura, T., 2016. Biometric assessment of deep-sea vent megabenthic communities using multi-resolution 3d image reconstructions.

714 Deep-Sea Res. Part I: Oceanogr. Res. Pap. 116, 200–219. URL: <https://www.sciencedirect.com/science/article/pii/S0967063>
715 716301091, doi:10.1016/j.dsr.2016.08.009.

716 Thornton, B., Ura, T., Nose, Y., Turnock, S., 2007. Zero-g class underwater robots: Unrestricted attitude control using control moment gyros. IEEE
717 J. of Ocean. Eng. 32, 565–583. doi:10.1109/JOE.2007.899274.

718 UK Government, 2020. New plans to make uk world leader in green energy. <https://www.gov.uk/government/news/new-plans-to-make>
719 -uk-world-leader-in-green-energy. (accessed 30 July 2021).

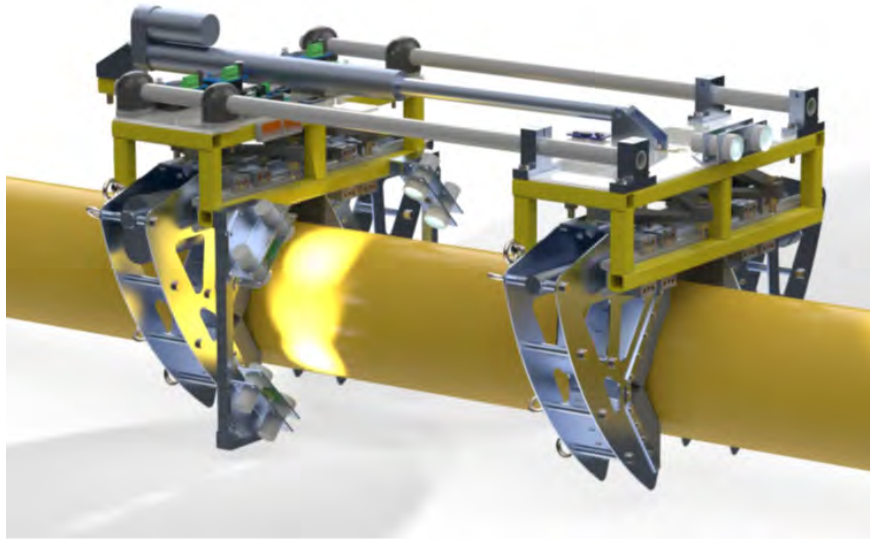
720 White, N., 2008. Semibalanus balanoides an acorn barnacle. Mar. Life Inf. Netw.: Biol. and Sensit. Key Inf. Rev. URL: <https://www.marlin.a>
721 c.uk/species/detail/1376.

722 Willner, D., Chang, C.B., Dunn, K.P., 1976. Kalman filter algorithms for a multi-sensor system, in: IEEE Conf. on Decis. and Control includ. the
723 15th Symp. on Adapt. Process., pp. 570–574. doi:10.1109/CDC.1976.267794.

724 Young, D., 2018. Predicting Dynamic Subsea Cable Failure for Floating Offshore Wind. Technical Report. ORE Catapult. URL: [https:](https://ore.catapult.org.uk/app/uploads/2018/09/Predicting-Dynamic-Subsea-Cable-Failure-for-Floating-Wind-David-Young-AP-0016-.pdf)
725 [//ore.catapult.org.uk/app/uploads/2018/09/Predicting-Dynamic-Subsea-Cable-Failure-for-Floating-Wind-](https://ore.catapult.org.uk/app/uploads/2018/09/Predicting-Dynamic-Subsea-Cable-Failure-for-Floating-Wind-David-Young-AP-0016-.pdf)
726 David-Young-AP-0016-.pdf.

727 Young, D., Ng, C., Oterkus, S., Li, Q., Johanning, L., 2018. Predicting failure of dynamic cables for floating offshore wind, in: Proc. of the 3rd Int.
728 Conf. on Renew. Energ. Offshore (RENEW 2018), October 8-10, 2018, Lisbon, Portugal, pp. 821–828.

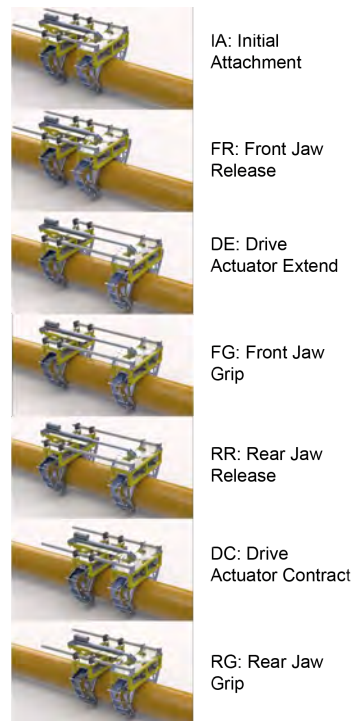
729 Zolich, A., Palma, David, a.K.K., Fjørtoft, K., Sousa, J., Johansson, K.H., Jiang, Y., Dong, H., Johansen, T.A., 2019. Survey on communication and
730 networks for autonomous marine systems. J. Intell. Robot. Syst. 95, 789–813. doi:10.1007/s10846-018-0833-5.



(a)

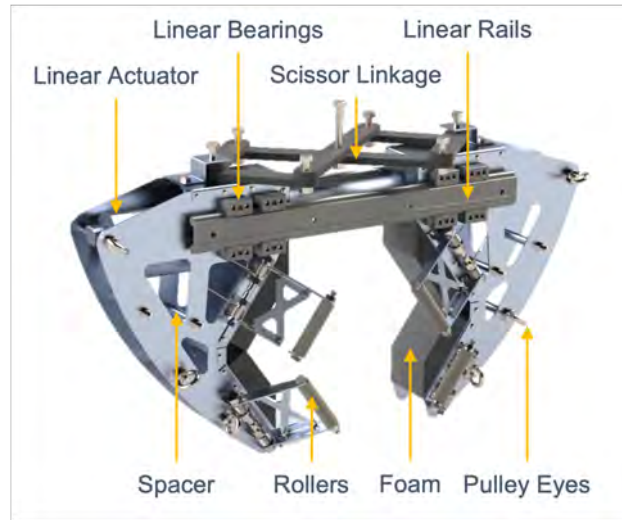


(b)

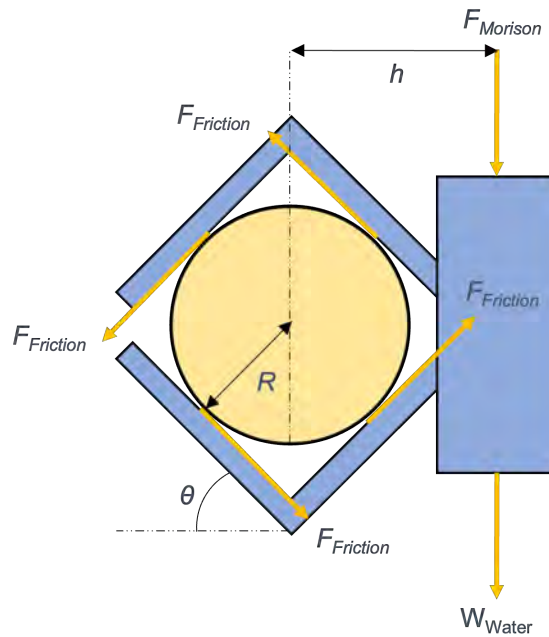


(c)

Figure 3: Proposed Autonomous Riser Inspection System (ARIS) design, showing (a) isometric view of a 3D CAD model, (b) photograph of the full-scale prototype developed and tested in this paper, and (c) the stages of the drive cycle.



(a)



(b)

Figure 4: Jaw unit design showing (a) general arrangement and (b) attachment force diagram.

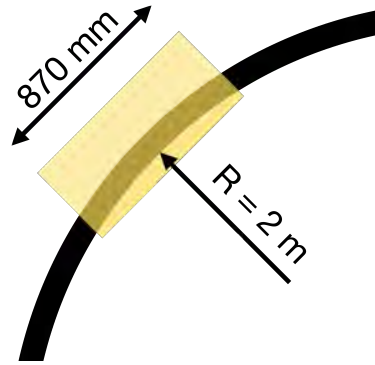


Figure 5: Illustration of the robot concept in this work in its fully extended position on a section of cable with a 2 m radius of curvature.

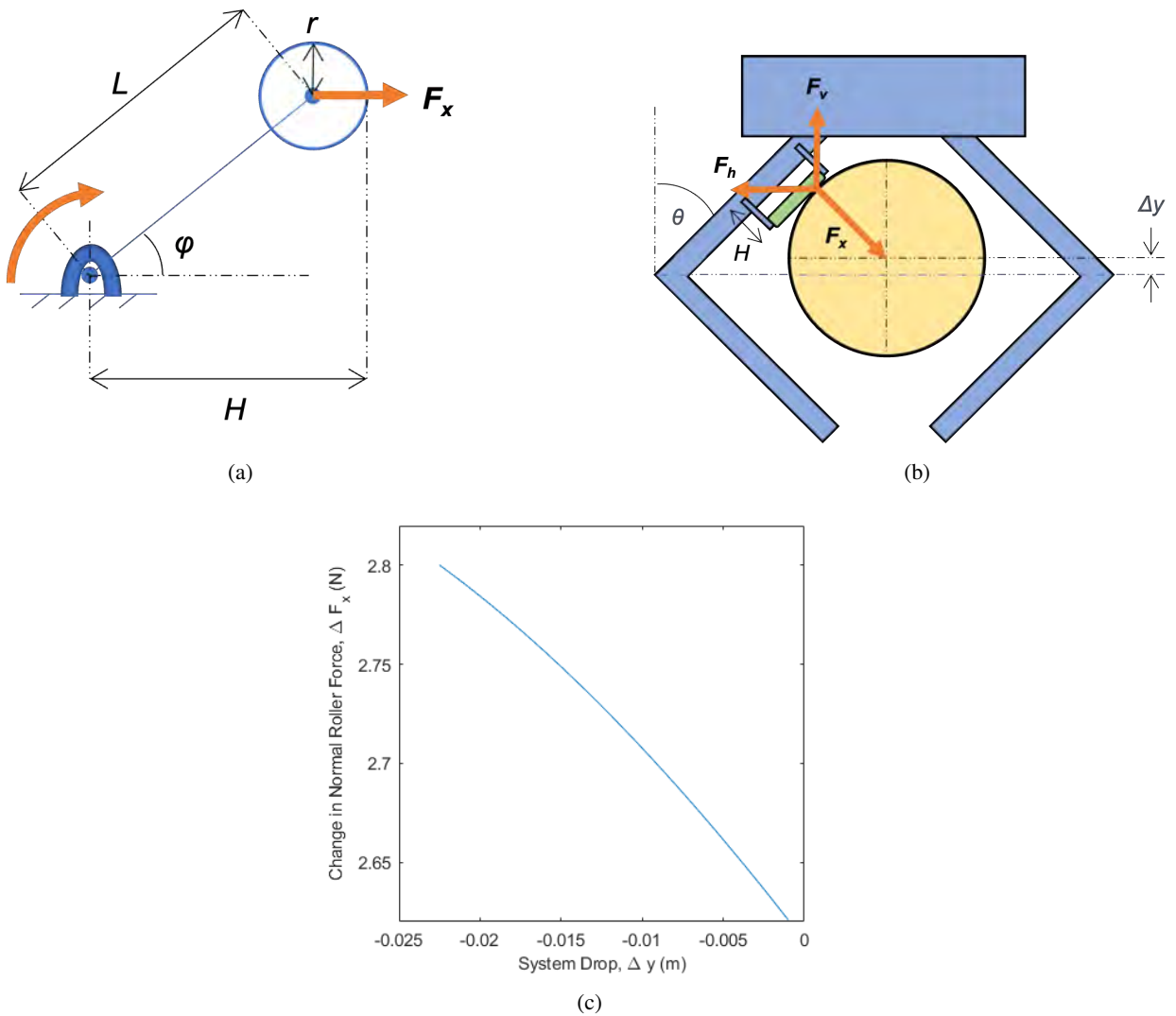


Figure 6: The forces exerted by the rollers, shown (a) from the side and (b) rear. (c) A graph showing the change in normal force exerted by a roller as a function of Δy given the parameters in Table 3.

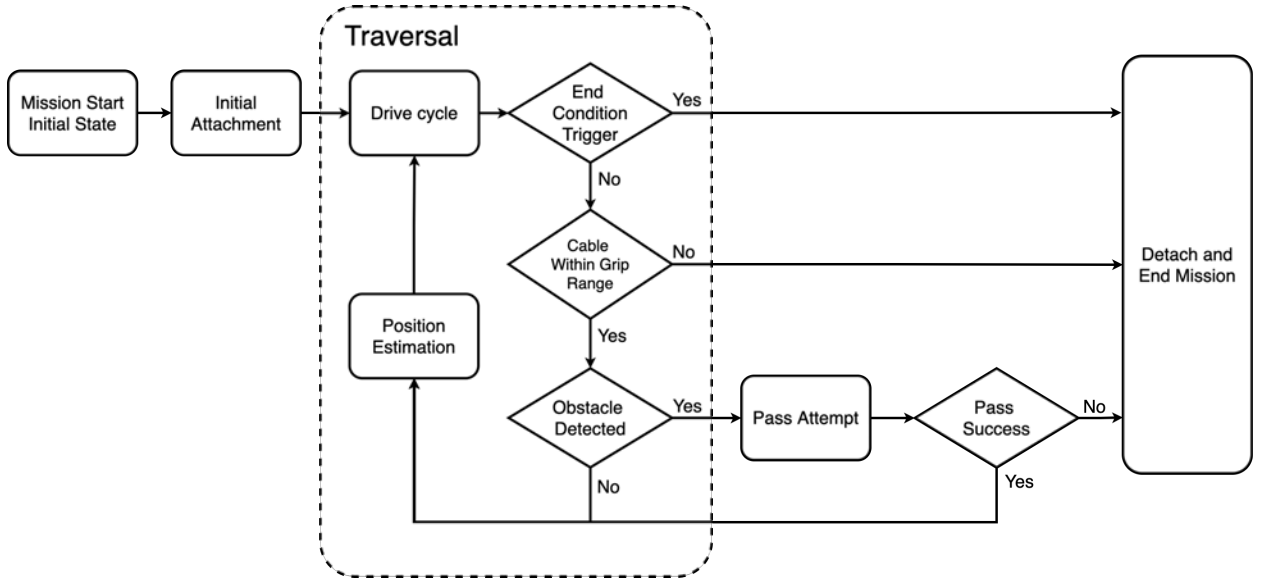


Figure 7: Autonomous mission flowchart. The robot starts its mission in its initial state, with both jaws fully open and the drive actuator fully contracted. Once it detects the cable using its ultrasonic sensors, it grips with both jaws and starts traversing the cable. During each drive cycle, the robot uses a combination of its ultrasonic sensors, actuator electrical current sensors and cameras to detect any abnormalities (e.g., unexpected detachment, obstacles) or if a mission end condition is triggered. Each of these events trigger an appropriate behavioural response for robust performance.

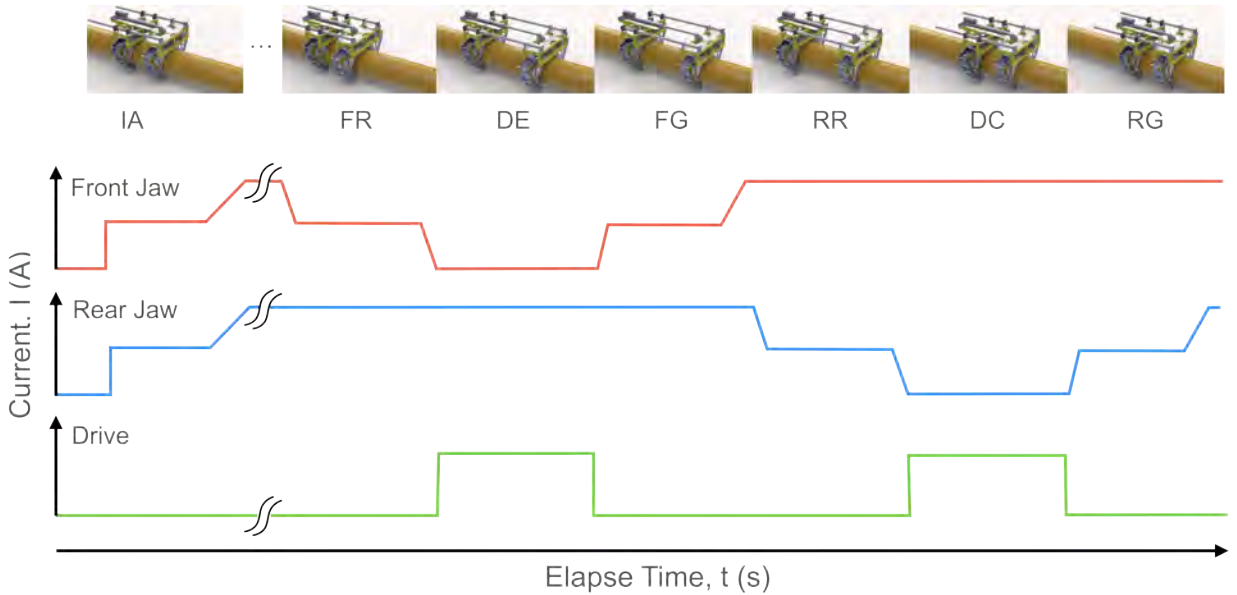


Figure 8: Expected currents drawn by each actuator during each stage of a drive cycle. The stages are labelled with the abbreviations defined in Figure 3.

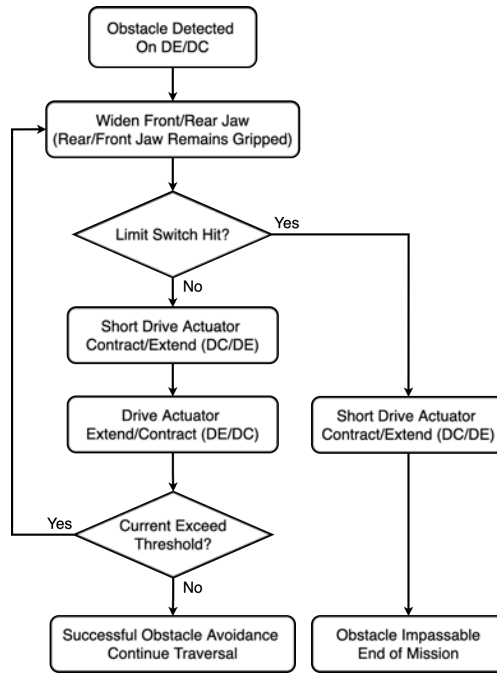
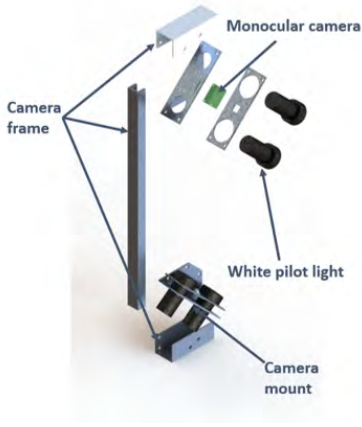
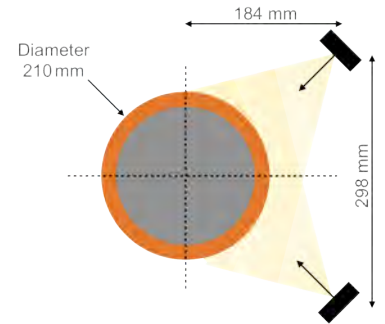


Figure 9: Flow chart for obstacle avoidance.



(a)



(b)

Figure 10: Visual inspection system showing (a) the frame that holds the cameras, and (b) the position of the cameras in relation to the cable.



Figure 11: A simulation showing the tracking of features to achieve visual odometry.

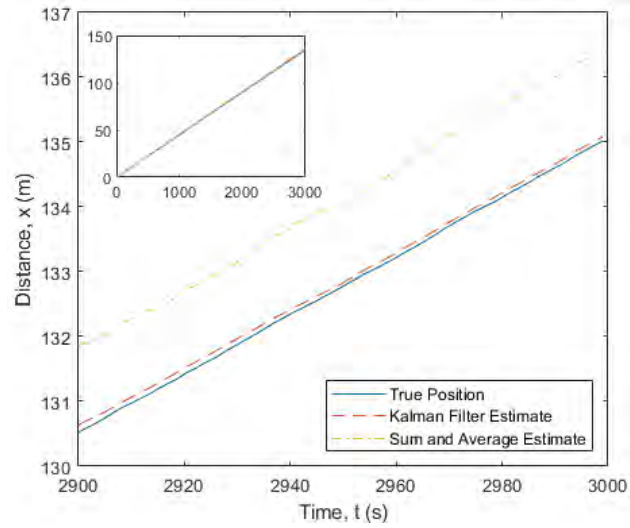
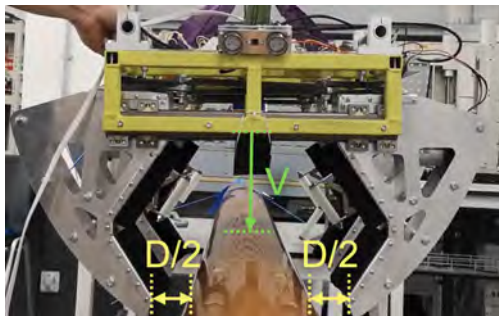
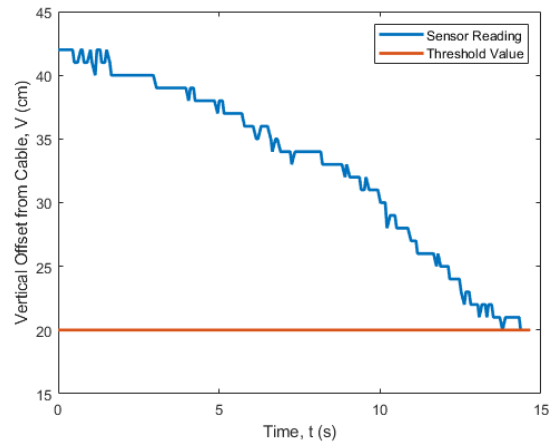


Figure 12: Position estimation error against time for a simulation of constant velocity traversal using a simple average of sensor inputs and the proposed KF.



(a)



(b)

Figure 13: Test rig for demonstrating autonomous initial attachment. (a) An ultrasonic sensor measures the distance to the cable V, where D represents the maximum position uncertainty that can be overcome by the system for a cable with 210 mm diameter. (b) A graph showing the ultrasonic data range recorded by the system and the threshold value required for attachment initiation.

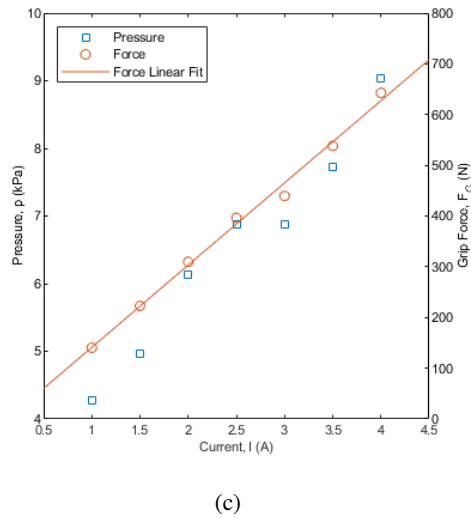
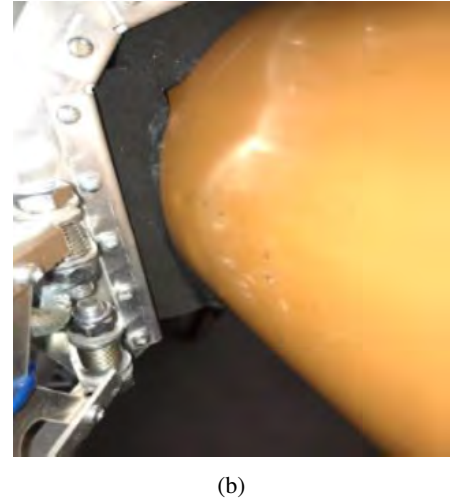
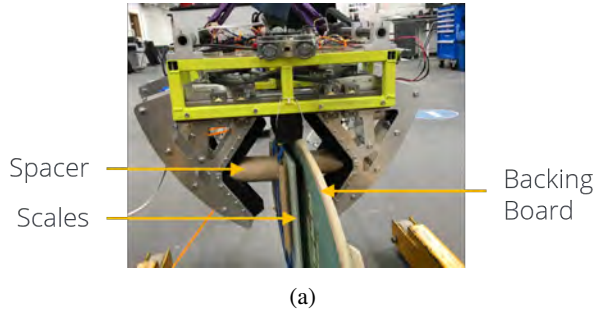


Figure 14: Experimental set-up for (a) force measurement, (b) the maximum contact area scenario, and (c) a graph showing results of force and pressure exerted at a range of actuator currents.

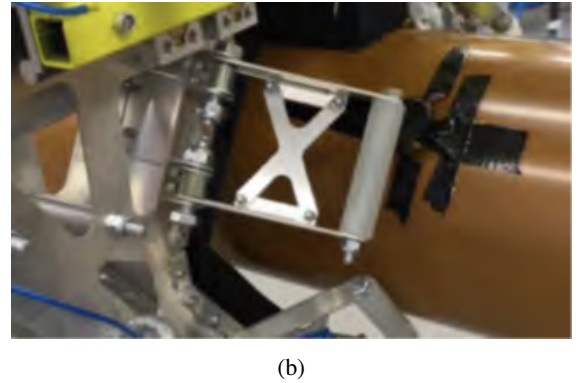
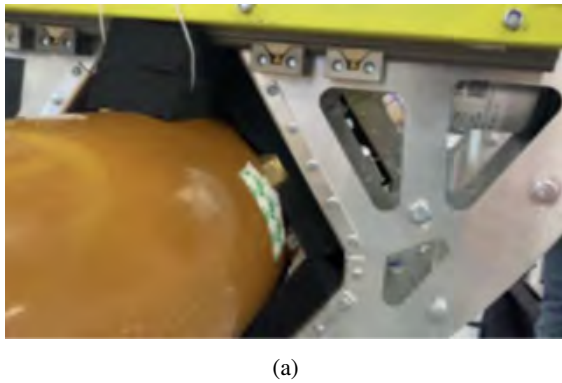


Figure 15: Gripping and traversal over a small obstacle, with (a) the compliant jaw interface material deforming around the model barnacle and (b) a roller traversing the obstacle during a drive cycle.

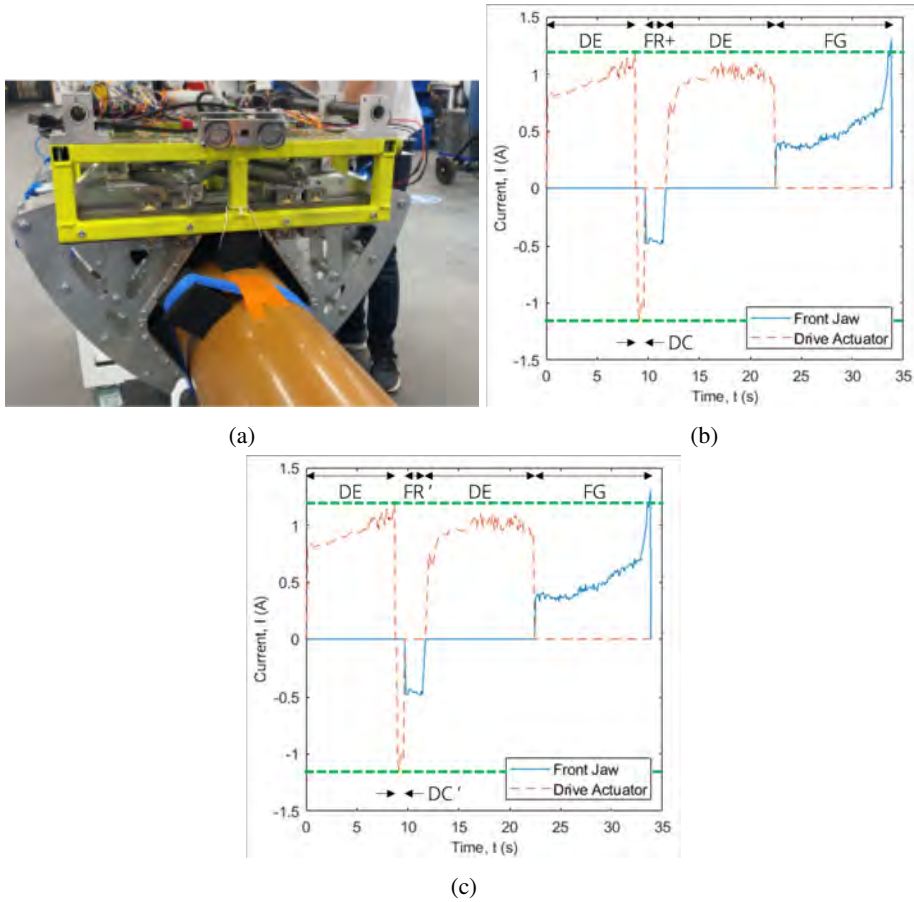
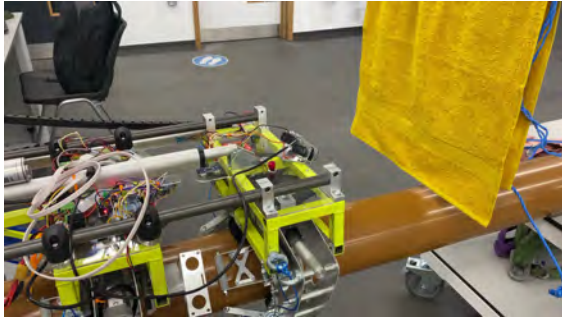


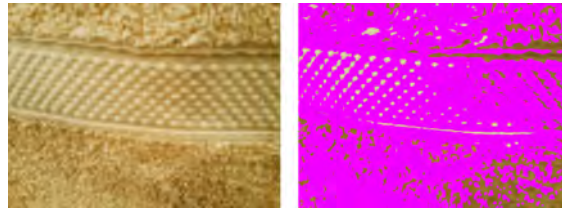
Figure 16: Obstacle avoidance experiments showing (a) the test setup, (b) the current for each actuator during a standard drive cycle, and (c) the current for each actuator during a pass attempt following the obstacle avoidance workflow (Figure 9). Drive cycle stages are defined in Figure 3, where FR' and DC' indicate small front jaw opening and drive actuator contraction. Negative currents indicate jaws opening and drive actuator contracting. The green lines indicate the obstacle detection threshold for the drive actuator.



(a)



(b)

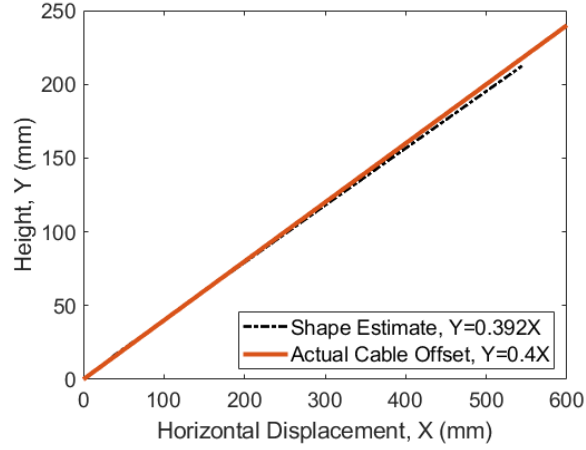


(c)

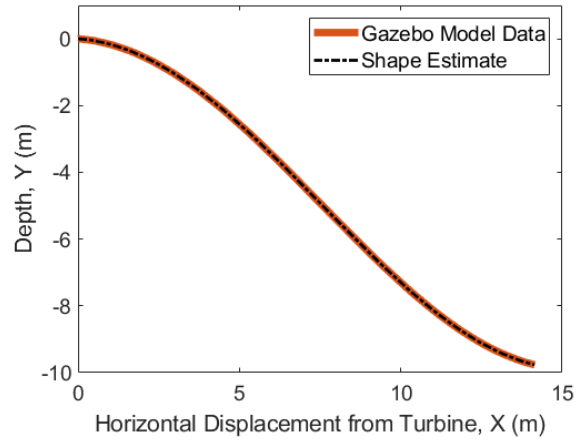
Figure 17: Buoy module detection experiments showing (a) the setup to verify visual processing performance, (b) the forward looking camera image at approximately 400 mm range to the buoy, showing the original image (left) and the detected pixels (right), where the sum of detected pixels makes up 38 % of the image frame and (c) forward looking camera image at approximately 100 mm range to the buoy, showing the original image on the left and the detected pixels shown in purple on the right, where the sum of detected pixels makes up 83 % of the image frame.



Figure 18: Edge detection results on the physical test rig.

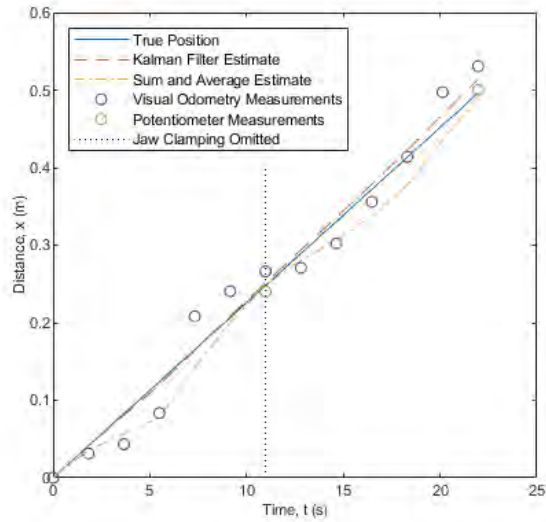


(a)

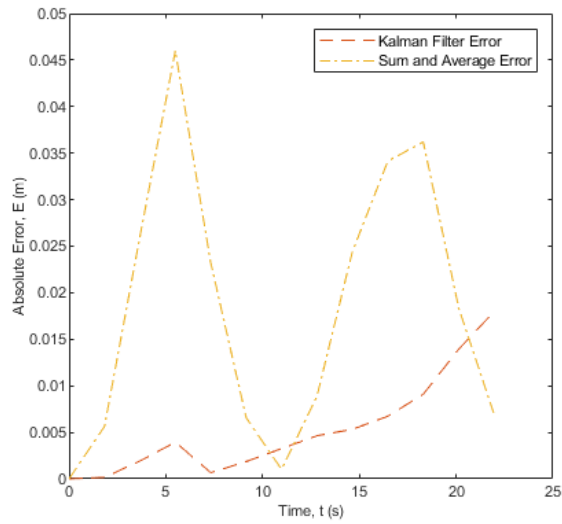


(b)

Figure 19: Cable shape estimation, (a) comparing estimates from recorded IMU data versus the actual slope of the cable test rig and (b) comparison of the cable shape estimate from simulated data versus the actual shape of the simulated cable model.



(a)



(b)

Figure 20: Traversed distance estimation (a) showing the distance traversed against time plotted over two drive cycles. The jaw clamping period is omitted at the black vertical line. The true position is compared with the sum and average and KF estimates. (b) A comparison of the absolute errors for the sum and average and KF methods shows that the use of KF offers more reliable estimates of traversed distance over the two cycle manoeuvre.